

# Role of Helium-Hydrogen ratio on energetic interchange mode behaviour and its effect on ion temperature and micro-turbulence in LHD

C.A. Michael<sup>1,2\*</sup>, K. Tanaka<sup>2,3</sup>, T. Akiyama<sup>2,4</sup>, T. Ozaki<sup>2</sup>, M. Osakabe<sup>2,4</sup>, S. Sakakibara<sup>2</sup>, H. Yamaguchi<sup>2</sup>, S. Murakami<sup>5</sup>, M. Yokoyama<sup>2,4</sup>, M. Shoji<sup>2</sup>, L.N. Vyacheslavov<sup>6</sup> and LHD experimental group<sup>2</sup>

<sup>1</sup>*Australian National University, Canberra, A.C.T. 2601, Australia*

<sup>2</sup>*National Institute for Fusion Science, National Institutes of Natural Science, 322-6 Oroshi-cho, Toki, Japan 509-5292*

<sup>3</sup>*Department of Advanced Energy and Engineering, Kyushu University, Kasuga, Fukuoka 816-8580, Japan*

<sup>4</sup>*SOKENDAI (The Graduate University for Advanced Studies), Toki, Gifu 509-5292, Japan*

<sup>5</sup>*Department of Nuclear Engineering, Kyoto University, Kyoto 615-8540 Japan and*

<sup>6</sup>*Budker Institute of Nuclear Physics SB RAS, 630090, Novosibirsk, Russian Federation*

(Dated: 4th June 2021)

In the Large helical device, a change of energetic particle mode is observed as He concentration is varied in ion-ITB type experiments, having constant electron density and input heating power but with a clear increase of central ion temperature in He rich discharges. This activity consists of bursty, but damped energetic interchange modes (EICs, X Du et al., Phys. Rev. Lett. 114 p.155003 (2015)), whose occurrence rate is dramatically lower in the He-rich discharges. Mechanisms are discussed for the changes in drive and damping of the modes with He concentration. These EIC bursts consist of marked changes in the radial electric field, which is derived from the phase velocity of turbulence measured with the 2D phase contrast imaging (PCI) system. Similar bursts are detected in edge fast ion diagnostics. Ion thermal transport by gyro-Bohm scaling is recognised as a contribution to the change in ion temperature, though fast ion losses by these EIC modes may also contribute to the ion temperature dependence on He concentration, most particularly controlling the height of an “edge-pedestal” in the  $T_i$  profile. The steady-state level of fast ions is shown to be larger in Helium rich discharges on the basis of a compact neutral particle analyser (CNPA), and the fast-ion component of the diamagnetic stored energy. These events also have an influence on turbulence and transport. The large velocity shear induced produced during these events transiently improves confinement and suppresses turbulence, and has a larger net effect when bursts are more frequent in Hydrogen discharges. This exactly offsets the increased gyro-Bohm related turbulence drive in Hydrogen which results in the same time-averaged turbulence level in Hydrogen as in Helium.

## I. INTRODUCTION

The differences of confinement of H and D plasmas, the so-called “isotope effect” in Tokamaks, reversed-field pinches (RFPs) and Stellarators/Heliotrons has long been a largely theoretically unresolved problem. In Tokamaks and RFPs, Deuterium is almost always noted to have better confinement than Hydrogen [1, 2]. However, the main scaling law for confinement, so-called Bohm or Gyro-Bohm scaling laws predict that Deuterium should have worse confinement due to a larger gyro-radius [3]. One mechanism considered to relate to this is the change in damping rate of geodesic acoustic modes (GAMS). [4]. On the other hand, in Stellarators, early experiments in W7-AS [5] suggested that there was only a very modest (20%) increase in electron temperature in Deuterium, and a database confinement study found virtually no difference in the ISS-normalized energy confinement time between Deuterium and Hydrogen in W7-AS, Heliotron-E and the ATF torastron [6]. Furthermore, improved particle transport in Deuterium has been reported in CHS [7] and Heliotron-J [8]. Recently there has been an impetus to study these effects on the Large Helical Device (LHD), which has

motivated the planned Deuterium campaign. Prior to starting this, a series of experiments were conducted in order to make a comparison of H and He discharges, which may give insight into both mass (A) and charge (Z) dependencies of transport (in particular the gyro-Bohm dependence which goes as  $\sqrt{A}/Z^2$ ), heating and instabilities. This has been the focus of several recent investigations of heat transport in the Large helical device [9], examining the role ion density (which reduces relative to electron density as the mass increases), absorbed heating power and transport, both neoclassical and turbulent. It was found that the collisionality dependence was much stronger than the ion species effects, such that at high collisionality, the ion-species had little distinguishable effect [9]. However, at low collisionality, characteristic of the ion-ITB type mode [10], the ion temperature increases with Helium concentration, by an amount significantly exceeding the gyro-Bohm scaling factor, particularly towards the edge [9]. It was shown [11] that this could not be explained by change of heating power, as this was mostly independent of He concentration, despite the ion density going down. It was shown in [12] that the change of  $T_e/T_i$  could contribute to this increase in confinement. The properties of turbulence in these discharges were analysed in [9, 12] and it was shown that the time-averaged density fluctuation profile, measured using phase-contrast imaging [13] was the same in both H and He discharges which is difficult to reconcile with the confinement improvement. In

---

\* C.A. Michael was a visiting associate professor from June to July 2016.

addition to the properties of heating and confinement, there is the possibility that energetic particle instabilities, driven by strong NBI heating, can also be affected by change of species.

Energetic particle instabilities, such as toroidal and beta-induced Alfvén eigenmodes (TAEs and BAEs) and fishbones are known to significantly degrade the population of NBI or ICRF-heated ions in Tokamaks [14]. Fast-electron driven instabilities have also been identified, including e-TAEs [15], e-BAEs [16] and e-fishbones [17]. Additionally, according to simulation, micro-turbulence driven by spatial gradients of bulk plasma properties (ion temperature) can also lead to a loss of energetic particles [18]. In fact, it is essential for heat transport analysis to validate predictions of plasma heating using neutral beams and ICRH based on fast ion measurements using well-established absolutely calibrated diagnostics such as fission chambers [19]. However, in Stellarators and Heliotrons, such systems are less mature in part owing the complexity in modelling and measurement of fast ions. On LHD, several types of energetic particle instabilities have been identified, for example TAEs, GAEs [20], EAEs, fishbones [21], and E-GAMS [22] which are also in the range of frequency of BAEs. Recently, however, a new type of fast ion instability was discovered, the energetic particle interchange mode (EIC) which results from a resonance of the precession frequency (which is around 7kHz for the  $m=1, n=1$  mode) of perpendicularly-injected fast ions ( $E=34\text{keV}$ ) with the resistive interchange mode which is located at around  $r/a=0.85$ , near the  $\iota = 1/1$  rational surface [23–26]. These tend to occur in low density plasmas ( $n_e < 1.5 \times 10^{19}\text{m}^{-3}$ ) and are common at high heating power of perpendicular neutral beam injection [23]. These modes tend to be bursting in time (repeating at various intervals in the order of  $\sim 0.1\text{s}$ ), lasting around 2-3ms, and exhibit chirp-down behaviour associated with a non-linear wave/particle interaction. Associated with fast ion redistribution, the plasma potential and toroidal rotation were shown to change dramatically within each burst.

In this paper, it is shown that EIC modes exist in the ion-ITB discharges used for comparing ion species effects, but are “damped” in that only a single oscillation spike exists (at around 7-8kHz), and that the perturbation is localized both poloidally and toroidally. It was shown in [23] that this behaviour tends to occur near the marginal boundary of existence of these modes (at higher density or marginal power). These burst rate of these modes decreases in He-rich discharges where  $T_i$  is higher, which may give clues as to the stability threshold for this mode. Also in these discharges, a steady 30kHz mode is found, with  $m=4, n=1$  mode structure. Although it seems like the 4th harmonic of an EIC mode, it does not fit the resonance condition for deeply trapped perpendicularly-injected fast ions as the mode propagates in the electron diamagnetic direction, whilst the trapped ions precess in the ion-diamagnetic direction.

It is vital also to consider how the fast ion pop-

ulation varies with He concentration, which could be either directly as a consequence of the CX neutral losses of energetic ions, or even the change of confinement associated with the gyro-Bohm scaling. Consideration is also given to the direct losses associated with the MHD modes. Analysis of the fast ion population is carried out by comparing CNPA signals, as well as the diamagnetic stored energy. The main tool for investigation is the 2D phase-contrast imaging system [13] which was analysed with very narrow time window ( $< 0.1\text{ms}$ ) and reveals dynamics in terms of large changes of the phase velocity of turbulence, which, given it is dominated by  $E \times B$  drift, indicates the  $E_r$  arising due to the fast ion losses and/or redistribution. Turbulence is suppressed during the bursts as reported in previous work [9, 24], and an analysis is carried out to link these observations with the confinement improvement in He.

This paper is organised as follows. In Sec II, the reference discharges are presented including the change of ion species concentration and temperature, together with previous studies on transport, turbulence measurements gyro-kinetic simulations. In Sec. III, the observations of the fast-ion MHD events are presented, focusing on changes to the phase velocity of PCI measurements, and results are presented on how these change with the Helium concentration, and the frequency and mode numbers are analysed. Also, evidence is presented to demonstrate the loss of fast ions during these events. A detailed analysis of the temporal modulation of turbulence amplitude and electron temperature by the MHD bursts is carried out, focusing on transport improvement. In Sec IV, we examine how the fast ion distribution, most particularly, the component driven by perpendicular NBI, changes with Helium concentration, based on NPA and diamagnetic loop signals. In Sec V, we discuss physics issues raised by these observations, looking at background neutrals, the fast ion distribution function, drive damping sources for this mode, and we unify the evidence for the EIC’s influence on ion heating. Finally, in Sec. VI conclusions are presented.

In this paper, we utilize the cross-covariance  $R_{xy}(L)$  for a given lag  $L$ , between the two variables  $x$  and  $y$ . We define the conventional correlation  $\gamma_{xy}(L)$ , the correlation  $\gamma_{xy}^{chg}(L)$  which quantifies how a change in  $x$  occurs after averaging over a series of bursts in variable  $y$  (for which we use phase velocity at  $\rho = 0.75$ ), and  $\gamma_{xy}^{rel}(L)$ , the normalization which represents the relative change in  $x$  :

$$\gamma_{xy}(L) = \frac{R_{xy}(L)}{\sqrt{R_{xx}(0)R_{yy}(0)}} \quad (1)$$

$$\gamma_{xy}^{chg}(L) = \frac{R_{xy}(L)}{\sqrt{R_{yy}(0)}} \quad (2)$$

$$\gamma_{xy}^{rel}(L) = \frac{R_{xy}(L)}{\bar{x}\sqrt{R_{yy}(0)}}. \quad (3)$$

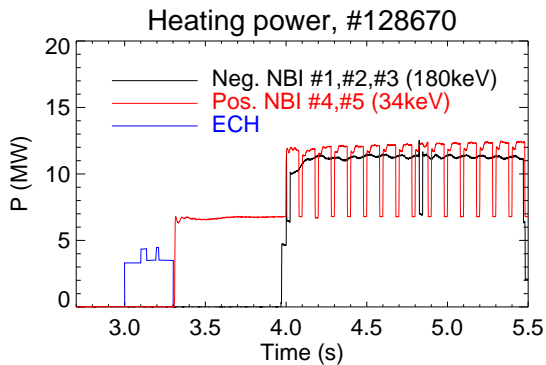


Figure 1. Heating power waveform, which is the same in all H/He comparison discharges.

## II. ION-ITB COMPARISON DISCHARGES

The targeted scenario for these comparison discharges was one with an ion internal transport barrier (ITB) [27, 28], where the strong ion heating results in high ion temperature, and the generation of ion temperature gradient (ITG) modes at mid radius. However, the transport “barrier” is considered to be due to a reduction of the gyro-Bohm normalized ion thermal conductivity at mid radius [28]. Subsequent to these discharges, the ion heating power was upgraded to provide further heating from an additional low energy positive-ion based neutral beam injection system. The heating waveform for this study is presented in Fig. (1). There are five Hydrogen neutral beam injection systems on LHD, with three of them injecting in the tangential direction to the field, and two of them injecting perpendicularly, with one of these beams being modulated at 10Hz (80ms on, 20ms off) for CXRS background measurement to obtain ion temperatures. For these shots, the perpendicular beams have an energy of 39-45keV whilst the tangential beams have an energy of 164-178keV (varying between each beam source but not between discharges)[29]. These high energy beams are well above the “critical energy” and deposit most of their power into electrons, whilst the low energy beams deposit most of their absorbed power into ions. For the perpendicular beams, there can be a relatively large shine through fraction, particularly at lower densities, because of the small path length through the plasma, and the tendency for fast ions with high pitch angle to be subject to prompt orbit loss. It is estimated that only 30% of the perpendicularly-injected neutral beam power is absorbed by ions.

Four discharges are highlighted where the neutral Helium concentration in the fuelling gas is varied, whilst the electron density is kept constant. The passive neutral spectral lines of He ( $\lambda = 587\text{nm}$ ) and H ( $\lambda = 656\text{nm}$ ) [30], which relate to the influx near the edge of the plasma, are used to measure the relative concentration of Helium in the discharge defined as  $c_{He} = n_{He}/(n_H + n_{He})$ , with  $c_H = 1 - c_{He}$  [31]. In fact, the ratio of H:He has been shown the

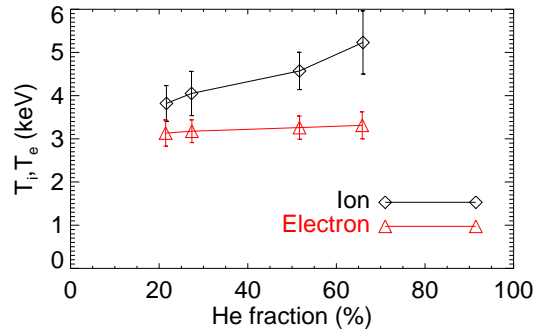


Figure 2. Dependence of electron and ion temperature (averaged over the core region  $\rho < 0.3$ , with variations conveyed in the error bar) on Helium concentration.

rather flat over the entire profile using CX spectroscopy [32]. The values of  $c_{He}$  vary from 20% to 70%, as neither Hydrogen or Helium could be completely pumped out of the vessel and walls. In these discharges, the line-averaged density exhibits different temporal dependence on account of the differing gas fuelling, however, feedback control brings the central line-averaged electron density to the same value at  $t=4.7\text{s}$ , and spatial profiles of electron density are also very well-matched. Further details of these discharges is discussed in Ref. [11]. Whilst the electron density is the same in all four discharges, the total density of Helium and Hydrogen ions are derivable from quasi-neutrality:

$$f_{He} = n_{He}/n_e = (1 - c_H)/(2 - c_H) \quad (4)$$

$$f_H = n_H/n_e = 2c_H/(2 - c_H) \quad (5)$$

From these equations, the total ion density fraction  $f_H + f_{He}$  decreases down to 1/2 with increase in He concentration, and is an important consideration in the analysis, particularly of the heating power per particle, as well as the contribution to the diamagnetic energy. The dependence of the core values of both  $T_i$  and  $T_e$  on He concentration is captured in Fig. (2). Clearly, the electron temperature does not change, whilst the ion temperature increases by  $\approx 30\%$  in He rich discharges. The first reason that may come to mind to explain this dependence is the reduction of the ion density in He rich discharges, leading to a higher power deposited per particle. However, using the TASK3D and GNET codes [11], it was shown that the reduction in ion density in Helium is offset by a decrease in the critical energy  $E_{cr} \sim (Z/A)^{2/3}$  (at which the ion and electron heating powers are equal), leading to less net power being coupled to the ions in He plasma.

A detailed analysis of the  $T_i$  profile, given in [9], shows  $L_{T_i}^{-1}$  is rather constant (and the same in He and H discharges) in the core regions ( $\rho < 0.9$ ), and increases in an “edge-pedestal” region. However, the height of the edge pedestal is larger in He discharges, leading by invariance of the core  $L_{T_i}^{-1}$  to a higher core  $T_i$ . This shows that ion transport is rather stiff

across the core regions so that the increase in  $T_i$  at the edge pedestal would contribute to raising  $T_i$  at the centre. Thus, the physics of edge temperature (heating, neoclassical, anomalous transport) are key to this dependence. As discussed, calculations of the heating power cannot explain the temperature difference [11].

Anomalous transport is expected to follow gyro-Bohm dependence  $\sqrt{A}/Z^2$ . Thus, it is natural to expect that the temperature would be greater by a factor of 2 in a Helium discharge for the same heating power (though other parameters such as ion temperature are part of the gyro-Bohm scaling). Transport analysis was carried out on these discharges in [9] to derive the net (power-balance) thermal diffusivity, as well as the neoclassical values. Surprisingly, the neoclassical contribution exceeded the net thermal diffusivity in the core, however it was concluded that the neoclassical values were untrustworthy in the presence of high beam power and strong external torque, and in fact the measured (rotation-based) radial electric field followed the electron root towards the core, contrary to the neoclassical predictions. Whilst it is possible from these calculations that the neoclassical contribution is non-negligible in these discharges, the presence of a critical gradient in the profile is good evidence that anomalous transport plays a significant role.

Considering the anomalous transport contribution, it is appropriate to normalise the transport coefficient with the gyro-Bohm scaling factor. It was shown in [9] that even after allowing for the gyro-Bohm factor, ion thermal transport in Helium discharge #128670 is lower than in Hydrogen discharge #128717 by a factor  $\sim 2$  times in the peripheral regions ( $\rho > 0.8$ ). Further detailed quasi-linear gyrokinetic analysis of the heat diffusivity in these discharges showed that the increase of  $T_i$  itself contributes partially to further reducing the gyro-Bohm normalised thermal diffusivity in He discharges, but is insufficient in peripheral regions to entirely explain this improvement. Additionally, it was shown that the experimental values of  $L_{T_i}^{-1}$  in H and He discharges were slightly above the critical gradient for ITG turbulence (which did not change between H and He, consistent with the experimental results over the inner radii), however, the linear growth rate above this threshold was lower in the He-rich discharge.

In summary, gyro-kinetic simulations qualitatively agree with the trend of the heat diffusivity vs He concentration as it exhibits a clear gyro-Bohm scaling. The calculated linear growth rate is lower in the He-rich discharge whilst the ion thermal diffusivity  $\chi_i = q/n\nabla T_i$  is also lower by ratio of the temperature gradient, given that the GNET [33] shows the power per particle to be the same in H and He discharges. On the other hand, the change of turbulence properties between H and He discharges is more complicated. According to quasi-linear theory, the fluctuation amplitude should be proportional to the growth rate, unless some other mechanism governing the saturation level changes such as the peak

wave-vector or zonal flow activity. Thus, one might initially expect the H discharge to have a higher level of turbulence. However, comparing the turbulence properties from the 2D-PCI system [13], using a long time interval (4.70-4.78s), it was shown that the amplitude profile was virtually identical between He and H rich discharges [11]. This inconclusive result has motivated a closer examination of 2D PCI signals, which revealed energetic particle-driven MHD bursts, with signatures appearing more clearly in PCI than any other diagnostic [9]. The burst rate is larger in the H rich discharge, and, given that these bursts result in a temporary suppression of the turbulence, may be the reason that the average level of turbulence does not increase for H-rich discharges, despite having a higher linear growth rate.

### III. BURSTING FAST-ION MHD ACTIVITY

#### A. Changes in turbulence and radial electric field

In these H/He comparison discharges, fast ion instabilities were identified with multiple diagnostics, but primarily the initial tool was a 2D phase contrast imaging system [13]. This diagnostic measures the line-integrated density fluctuations, and, through frequency and k analysis, also enables the phase spatial profile (mapped to flux coordinate  $\rho$ ) of the fluctuation amplitude, as well as the phase velocity profile  $V$  (perpendicular to the line of sight) to be obtained. An analysis of discharges in #128717 (The H-rich shot) was carried out considering very short time windows (0.1ms), as shown in Fig. (3). Consequently, only turbulence components with  $f > 10\text{kHz}$  have been considered. In this manner, 2D PCI can be used to deliver information about the time variation of the radial electric field with arbitrarily high time resolution (limited only by the bandwidth of the turbulence). The spectral density of fluctuations  $S(\rho, V)$  is plotted in Fig. (3a,b). The gap at  $-0.5 < \rho < 0.5$  is because the sight line does not penetrate to the magnetic axis. Furthermore, the sign of  $\rho$  denotes locations above (positive) and below the mid-plane (negative). It can be sensitive to the eddy tilt angle and so this can cause an apparent up/down asymmetry. The average velocity at each location is calculated using the moment over velocity, and is denoted by the solid line. Since the diagnostic measures only the component of the velocity perpendicular to the vertical probing beam, and since turbulence propagates in the poloidal direction (including  $E \times B$  and diamagnetic rotation components), the component of measured phase velocity is high near the edge of the plasma, reducing towards zero at the tangency radius, and inverting on the other side. The phase velocity is dominated by  $E \times B$  rotation, as has been shown in [9]. The key interpretation here is that turbulence phase velocity is dominated by  $E \times B$  rotation and so this can be a monitor at high time resolution of changes in electric field.

The comparison between Figs (3a) and (b) shows how the turbulence velocity spectra change spontaneously within a short period of time. Initially, the phase velocity is in the ion diamagnetic direction, which is typical for high  $T_i$  discharges, and then, it reverses spontaneously towards the electron diamagnetic direction. It is suggested that fast ion losses are responsible for the change of direction, and that this mode is very much like an energetic interchange mode, on the basis of magnetic probe measurements in Sec. (III B) and fast ion loss measurements presented in Sec. (III D). Whilst the poloidal rotation was not available in this discharge, heavy-ion beam-probe data indicates that in EIC events [23] that the radial electric field reverses during the burst. In addition, the symmetry of the turbulence signal changes. This is most likely to be due to a change in the eddy tilt angle, which results in constructive interference on the top and destructive interference on the bottom [34, 35]. This is a natural consequence of a change of a strong change in the  $E \times B$  shearing rate by the bursting mode.

Integrating over all velocity components gives a spatial profile of fluctuation amplitude, and, the bottom and top profiles are averaged and plotted as a function of time, together with the average phase velocity profiles in Fig. (3c,d). It is clear that there are several rapid changes in the phase velocity, large enough to shift the rotation from the ion to the electron diamagnetic direction. The turbulence amplitude is bursting up and down in this interval, and there is sufficient turbulence signal at all times to characterise the phase velocity. In fact, during the bursts, a slight reduction in the turbulence amplitude occurs. This effect will be analysed in more detail later. In Fig. (3e), the Logarithm of ratio of the fluctuation amplitude on top to that on the bottom is plotted, conveying how the eddy tilt angle changes dramatically during these bursts as discussed above.

These dramatic changes in the rotation velocity are likely to be due to a localized change in the radial electric field, and appear to have the signature of EICs, which are associated with fast ion losses and/or redistributions (shown in [23] by signatures in the HIBP and CXRS systems). The magnitude of the change in velocity with each burst is demonstrated more clearly using a narrow time interval in Fig. (4a) (where the phase velocity is offset from a particular time in-between the bursts), and compared the fluctuation amplitude profile evolution in Fig. (4b), as well as the a time evolution of the magnetic probe signal and wavelet spectrogram in Figs (4c,d). It is clear that the phase velocity (electric field) changes are clearly localized in the region  $\rho = 0.6 - 0.9$ , and turbulence amplitude is reduced in that time, though the asymmetry changes. These changes are broadly similar to the magnitude of the electric field change observed for an EIC, and is in the same negative radial direction (poloidally electron diamagnetic direction). In [23], it was shown that for EICs, the radial current associated with the outward movement of fast ions could be derived from

the time derivative of the electric field according to Faradays equation  $\nabla \times B = j + e dE/dt$  (assuming B doesn't change). It was argued that one can determined the loss current from the rate of change electric field in the build up phase of the event. On the other hand, in the recovery phase, the phase velocity decreases on a timescale related to the parallel-viscosity (shown in Fig. (4a)) [23].

## B. Magnetic probe signatures and mode identification

The magnetic probe signals (which measure  $dB_\theta/dt = \omega \tilde{B}_\theta$ ) show clear signatures of these bursts. In Fig (4c), the raw signal is shown for the He rich discharge, for one such burst event, separated out into high and low frequency components (above/below 25kHz), and in Fig. (4d), which shows a wavelet spectrogram. Low frequency components around 8kHz are present before the event, characteristic of resistive-interchange type activity. At the time of the burst, its amplitude increases and frequency broadens, but remains very transient, dying away after  $\sim 200\mu s$ . This is particularly evident in the low-pass filtered raw signal in Fig. (4c), which shows an increasing amplitude, but the peak remains there for only one cycle of the oscillation. Analysis of the Mirnov array indicates that this mode has a clear  $n=1$  structure, and a very low  $m$  number, between 0 and 1, which is similar to that observed at the onset of an EIC mode.

Both during and between events, a persistent (though bursty) mode around 30kHz is present. At the time of the bursts, this mode jumps up in frequency (to 40-50kHz) and amplitude followed by a chirp-down type behaviour. The toroidal mode number of the higher frequency 30-40kHz mode is found to be  $n=1$ , whilst the poloidal mode number is found to be  $m=4$ , and it propagates in the electron diamagnetic direction poloidally and clockwise direction toroidally (same as EIC). Furthermore, the poloidal propagation speed  $2\pi fr/m$  is roughly the same as that for the EIC since both the frequency and poloidal mode number are 4 times that for the EIC. The chirping up then down behaviour may be an influence of the change in plasma rotation velocity. Given that the PCI phase velocity is close to the plasma  $E \times B$  rotation velocity, the change in mode frequency can be computed from the simple formula  $\Delta f = \Delta v_{phase} m / (2\pi r_{eff})$  (neglecting changes in the toroidal rotation). This frequency is computed, offset from an initial value of 30kHz, and compared with the mode frequency in Fig. (4d). It is clear that this waveform, indicated by dashed line, closely matches the changes in mode frequency. However, there may be additional corrections owing to the intrinsic mode frequency. It has been suggested that this could be in the electron-diamagnetic direction [26].

Conventionally, if the mode were resonant at a rational surface with the resonant surface with  $\iota = \iota_*$ , that value would be given by  $\iota_* = n/m = 0.25$ .

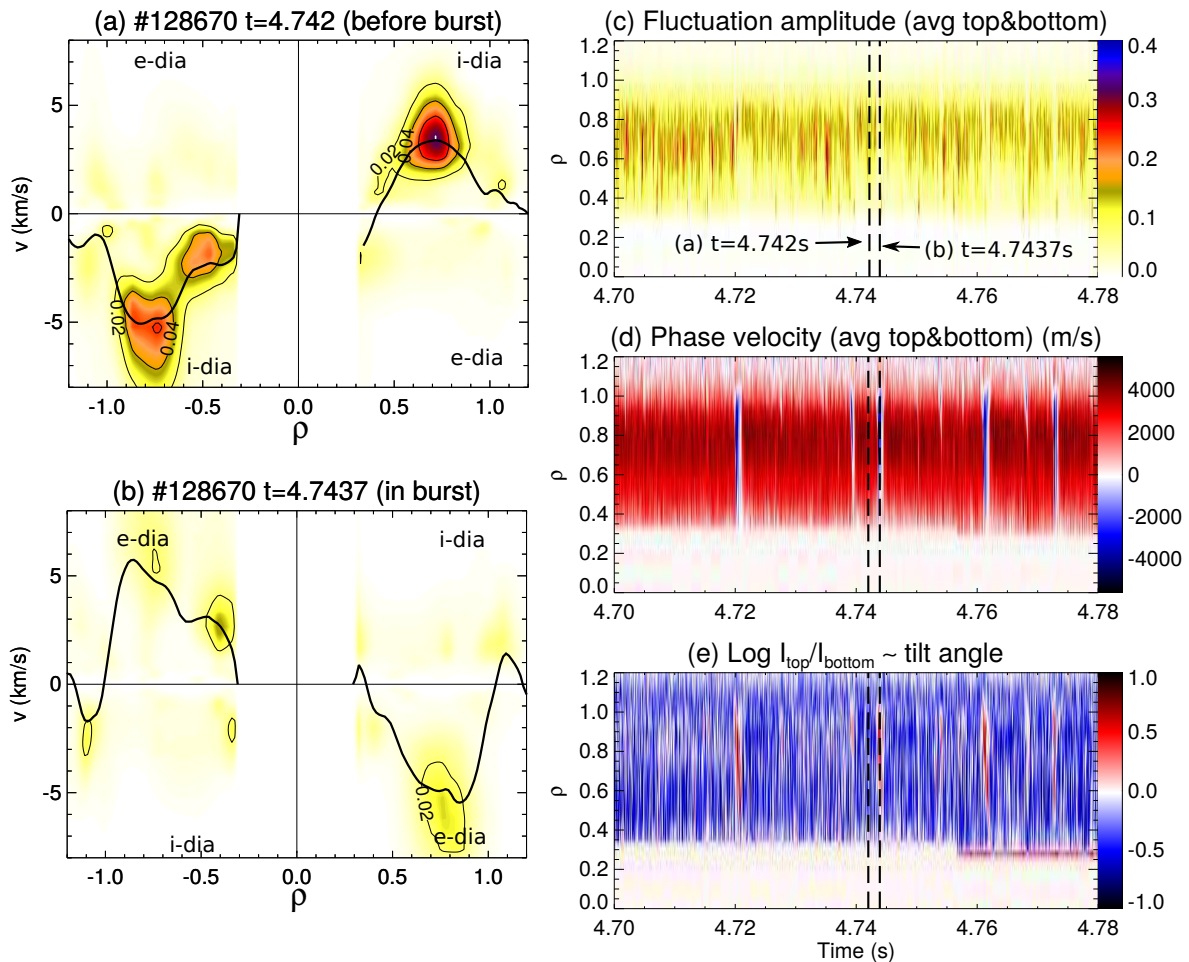


Figure 3. Turbulence spectral density  $S(\rho, V)$ , where  $\rho$  is the normalized radius (sign denoting which side of the mid-plane) and  $V$  is the phase velocity, at (a)  $t=4.742$ s and (b)  $4.7437$ s in He dominant discharge #128670 (same linear colour scale and contour levels). The line indicates the average phase velocity (projected perpendicular to vertical probing beam), which is taken to greatly represent the  $E \times B$  poloidal rotation velocity of the plasma. These are compared with the time histories of (c) fluctuation amplitude (linear colour scale) and (d) fluctuation phase velocity spatial profiles, averaged over the bottom and top halves of the profile, as well as (e) the amplitude asymmetry, which relates to the eddy tilt angle.

However, the minimum value of  $\iota$  is  $\approx 0.4$ , occurring in the centre of the plasma. As the  $\iota = 0.25$  surface is not present in the plasma, it suggests that this mode must have considerable  $k_{\parallel}$ . One possible explanation is that the mode is like Alfvén wave in 3D toroidal geometry, where gap locations can occur for a range of couplings to the poloidal and toroidal field harmonics  $(\mu, \nu)$  (with  $N = 10$  being the toroidal field periodicity of the Heliotron) [36]:

$$\iota_* = \frac{2n + \nu N}{2m + \mu}. \quad (6)$$

Considering possible values for field harmonics  $(\mu, \nu)$  as (2,1) and (1,1) for “helical ripple”, we can obtain  $\iota_* = 1.2, 1.33$  respectively, which are located at  $\rho = 0.9, 0.95$  respectively. Such couplings would put this mode into the family of the “helicity-induced Alfvén eigenmode” (HAE). Previously reported HAE modes were of higher frequency (in the range  $\approx 200$ kHz), as reported in [37], but gap mode solutions can exist over a broad range of frequencies.

Furthermore, the mode frequency is broadly in the range of  $\beta$ -induced Alfvén eigenmode (BAE) and the energetic particle GAM [22], but since  $v_A \sim 1/A$ , the frequency should change with He concentration, which is not the case. To determine what fast particles destabilise this mode, we have to consider the condition [38]:

$$f - (m + j\mu)f_{\theta} + (n + j\nu N)f_{\phi} = 0, \quad (7)$$

(with  $j = 0, \pm 1$ ), and  $f_{\theta}, f_{\phi}$  being the poloidal and toroidal precession frequencies. It is not possible for perpendicularly-injected beam ions to satisfy this resonance condition, despite having the same poloidal propagation velocity as the EIC, which is driven by these particles [23], because the mode propagates in the electron diamagnetic direction, whilst these fast ions precess in the ion diamagnetic direction. It was shown that for an EIC, coupling with field harmonics  $(\mu, \nu) = (0, 1)$  could create such a resonance in the ion diamagnetic direction, however no such condition can be found for the 30kHz



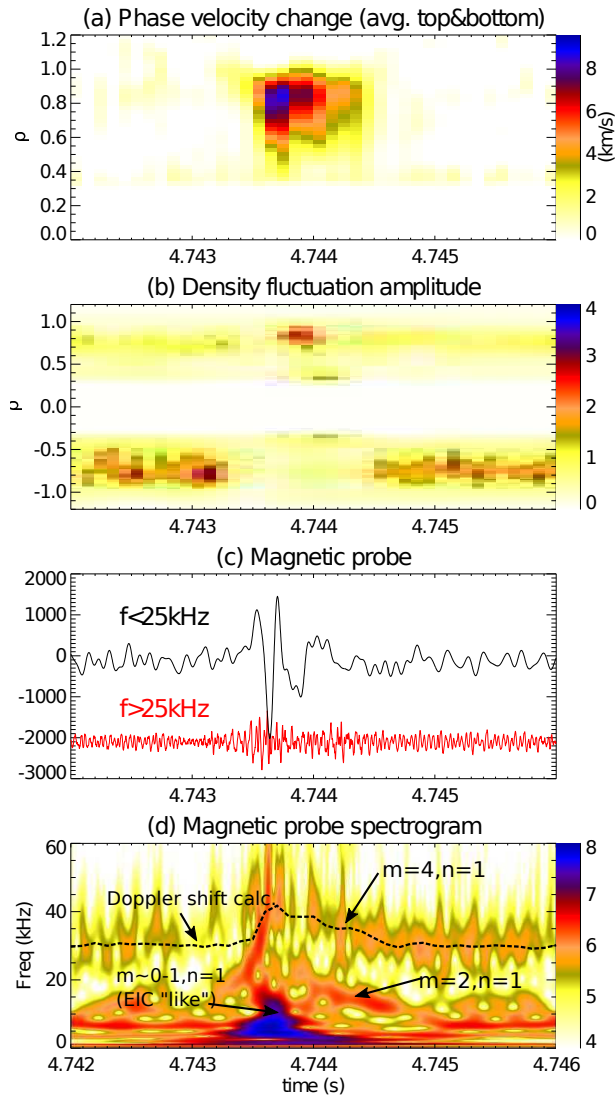


Figure 4. (a) Radial distribution of the change in PCI phase velocity (averaged over top and bottom) from the initial reference time for He-rich discharge #128670, compared with (b) the fluctuation amplitude, resolved over the top and bottom. (c) The magnetic probe ( $\dot{b}_\theta$ ) waveforms for frequency intervals above and below 25kHz, and (d) magnetic probe wavelet spectrogram (6<sup>th</sup> order Morlet). Arrows indicate the mode numbers for the respective mode branches, and the line indicates the Doppler shift frequency change (from the initial frequency of 30kHz) calculated using the phase velocity change in (a).

mode. Such a discrepancy has also been reported before. Reverse shear Alfvén eigenmodes in LHD also propagated in the electron diamagnetic direction contrary to expectations [39]. Whilst this mode does not appear to fit a resonance condition, the fact that its amplitude increases during EIC bursts, and the fact that the mode on-set occurs after perpendicular NBI injection as shown in Fig. (5b), suggests that it is driven by perpendicularly-injected fast ions. Whilst the nature and drive of the mode remains elusive, and further investigation is required to fully understand it, the EIC mode amplitude is distinctly greater than that of the 30kHz

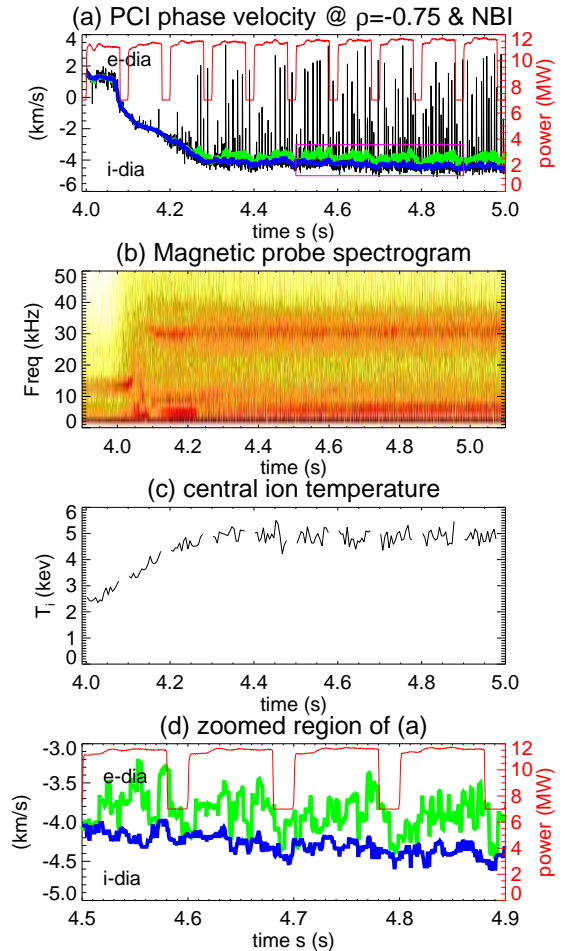


Figure 5. For 27% He concentration shot #128665: (a) Time history of phase velocity (black), as well (blue) as a running median filter over 10ms (blue), to remove spike features, and (green) a boxcar average filter, compared with perpendicular beam power (red). (b) Magnetic probe spectrogram. (c) Central ion temperature. (d) zoomed region of (a) to show how average phase velocity (green) reduces when beam power reduces

mode. From the mode amplitudes presented in Fig. (4), the magnetic probe (which measures  $dB_\theta/dt$ ) for the low frequency EIC mode is  $\sim 2\times$  that of the 30kHz mode. Considering the frequency dependence of the probe response, this means that the field perturbation would be around  $10\times$  larger. As shown later in Fig. (10c,d), in other discharges, the EIC mode amplitude is even higher relative to the 30kHz mode.

### C. Generation of bursts by Perpendicular NBI

The conditions which lead to the EIC bursts and the 30kHz mode can be examined by looking over a wide time interval. The phase velocity, together with the perpendicular NBI #4 current waveform, as well as the magnetic probe spectrogram and central ion temperature for the 27% He shot #128665 in

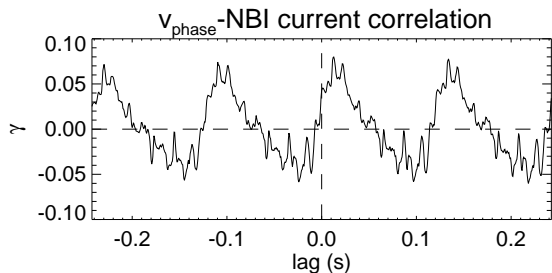


Figure 6. Cross-correlation function between the perpendicular NBI current, and the phase velocity, (minus a running median filter) demonstrating how the bursts in the phase velocity are also modulated by the NBI current.

Fig. (5). At  $t=4.0s$ , the perpendicularly-injected beam power increases from 7 to 12MW and is then modulated at 10Hz with a 80% duty cycle. The ion temperature starts to increase and reaches its equilibrium level at  $t = 4.3s$ . During the time interval  $t = 4 - 4.3s$ , the phase velocity at  $\rho = 0.75$  switches from the electron to ion diamagnetic direction. The bursting activity starts to commence around 4.1s although they start out small and do not reach their maximum magnitude until around 4.3s.

On the other hand, the 30kHz mode appears at  $t=4.1s$ . Given that the fast ion slowing down time is around 100ms, the 30kHz mode is triggered once the fast ions start to come into equilibrium with the bulk ions, but before the ion temperature has reached its maximum level. Thus we can conclude that the 30kHz mode is either destabilized by the ion temperature gradient, or by fast ions of energies and pitch angles which are different from the the birth injection and pitch angle, thus taking a slowing/scattering timescale in order to trigger the mode.

It also appears from a glance from Fig. (5a) that the phase velocity bursts are smaller and less regular in the 20ms intervals when the beam power is lower. Also indicated in Fig. (5a), a running median filter over 10ms is indicated in blue, which removes the bursting velocity features, to give a measure of the baseline variation of the phase velocity, as well as a boxcar average filter in green, which smooths over the spike features, but does not remove them. These traces are reproduced over a narrower region for clarity in Fig. (5d) to see their correlation with the NBI power. The difference between the green and blue curves demonstrates the time evolution of the bursting events. From these traces, it is clearer to see that bursting events reduce in the beam-off periods, and how the burst rate steadily increases in time when the beam is on.

The cross-correlation function between the phase velocity (corrected with the blue baseline in (a)) and perpendicular NBI current signals is plotted in Fig. (6). The waveform of the correlation function has a period precisely 0.1s which is the NBI modulation period, demonstrating again how the bursts evolve in time. Almost identical correlation signatures were

found in other He concentration shots. This indicates that the bursts, which is suggesting fast ion loss, is strongly affected by the perpendicular beam power.

#### D. Fast ion loss measurements

An examination of the response of various fast ion diagnostic systems (summarized in [40]) may confirm whether this bursting mode is associated with fast ion redistribution/losses. Several neutral particle analysers are available, which collect CX neutrals from the ambient neutral density. A Compact Neutral particle analyser measures the energy spectrum of such neutrals, being sensitive mostly to hydrogen [41]. The sightline for this diagnostic is vertical, mostly perpendicular to the field. As such, this is mostly sensitive to fast ions arising from perpendicular beam injection (NBI 4&5). Also, as shown later by spectra in Fig (12), signal is present at energies above the injection energy of the perpendicular beams (40keV), which is considered to be due to slowing down and pitch angle scattering of fast ions driven from the tangential injected NBIs (1,2,3) which have an injection energy of 180keV. A silicon FNA type detector (SiFNA) is also available which does not provide any energy resolution [42], and for these discharges provided spectra also from only a perpendicular sight line (however, in general, parallel sight lines are available). The radial location from which the signal arises with both of these passive NPA diagnostics is determined by the competing effects on one hand of the decreasing fast ion population towards the edge of plasma, and the decreasing neutral donor population towards the core of the plasma. Additionally, an RF spectrometer mounted on a manipulator measures ion cyclotron emission (ICE) [43] and its very high order harmonics [44], and is sensitive to the perpendicular energy of fast ions lost near the edge of the plasma.

A time history of the amplitude of these 3 fast ion diagnostics, as well as diamagnetic stored energy and magnetic probe signal separated out into components above and below 25kHz are compared with the fluctuation phase velocity and amplitude at  $\rho = 0.75$ , for the 30% He shot in Fig. (7). This simple line profile comparison creates a clear impression of the nature of these bursts. With each burst, the phase velocity changes suddenly in less than 0.1ms and reverses for about 2ms. During that time, the fluctuation amplitude decreases dramatically. At that time, the RF spectrometer channel at 300 and 400MHz has a clear increase in the signal. This diagnostic is considered to measure fast ions in the very periphery of the plasma, and thus conveys the redistributed (radially transport) fast ions to the edge of the confinement region of “lost” fast ions. Due to the complex nature of ICE emission, it is difficult to identify the position of this emission based on cyclotron frequency alone. Nor is not clear from that exactly how many fast ions are being lost. The CNPA and SFNA signal also have ap-



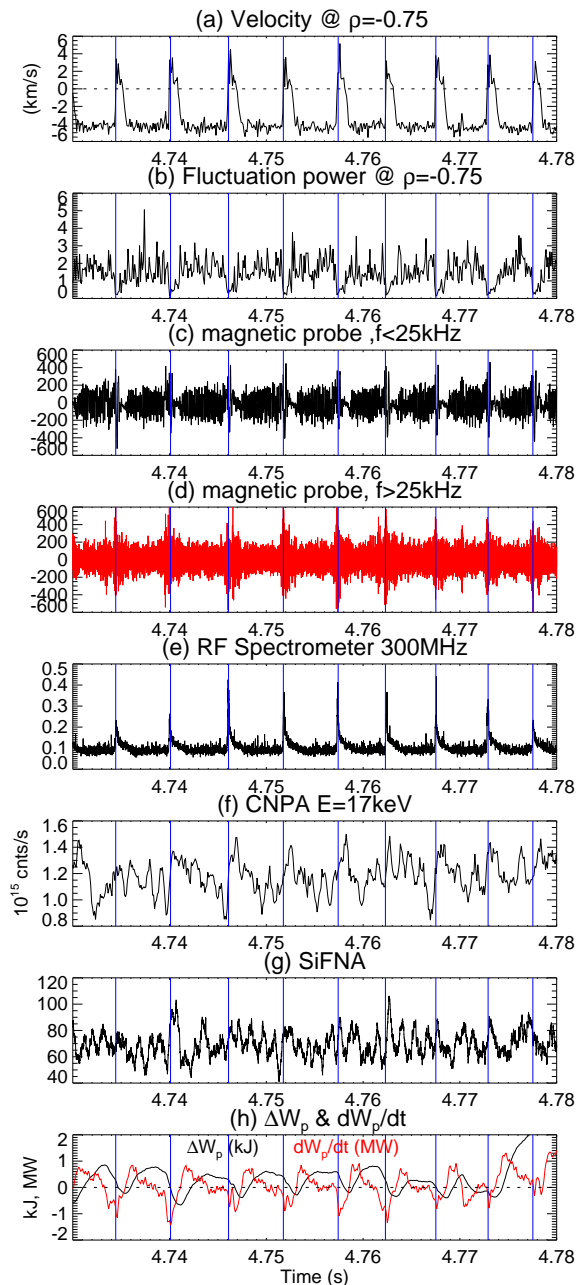


Figure 7. Time history of (a) fluctuation phase velocity and (b) amplitude at  $\rho = -0.75$ , compared with the raw magnetic probe signal ( $dB_\theta/dt$ ), low pass filtered (c) and high pass filtered (d) above 25kHz, (e) the RF ICE spectrometer with 300MHz energy channel, (f) the CNPA signal at 17keV, (g) the SiFNA signal and (h) changes of the diamagnetic stored energy (high pass filtered above 50Hz to remove the baseline variation), together with the time derivative (red) for the 30% He shot #128708.

parently positive spikes at the time of these bursts, however their correlation is much less obvious than with the ICE spectrometer. Nonetheless, a positive spike may be due to the redistribution of fast ions further towards the edge of the plasma where the donor neutral density is larger, or it may be as a result of increased background neutral density, as a consequence of the burst itself – which is possible

considering there is a slight drop of edge electron temperature, as shown in Sec. (III F), and no clear change in the electron density from the FIR interferometer.

To investigate this phenomenon in more detail, the cross-correlation  $\gamma^{rel}$  (as defined in Eq. (3)) between the PCI phase velocity and the fast ion diagnostics including the SiFNA, the CNPA and the RF spectrometer were evaluated in Fig. (8a-c). This analysis effectively averages over multiple events to detect the relative influence that these events have on the fast ion signals. Different energy channels for the CNPA are plotted, and, although the signal changes over orders of magnitude as a function of energy, as discussed later in Sec. (IV A), the relative change is independent of energy, increasing by about 10% with each burst, up to an energy of about 60keV at which point the SNR is not adequate. The initial conclusion from this graph is that fast ions are lost over a broad energy range, which is different to that shown in [23] where there was a distinct change in the character of the bursts around  $E_b = 35\text{keV}$  corresponding to the injection energy of the perpendicular beams. However, it could also be an effect of changing neutral density. The cross-correlation with passive  $H_\alpha$  monitors, shown in Fig. (8d) indicates that the passive neutral density goes up after the burst by about 1%, which is insufficient to explain the increase in the NPA signal. Therefore, radial fast ion redistribution must occur over a broad range to regions with higher donor neutral density.

Whilst none of the above signals convey the absolute magnitude of the amount of fast ions lost for each event, the diamagnetic loop, conveying the stored energy in the field perpendicular direction, is well calibrated, and is sensitive to the beam ions of NBI 4 and 5 which dominantly produce energetic particles with high perpendicular velocity. Moreover, it does have fast enough time resolution to see the influence of every burst event. The time history of the stored energy  $W_p$ , high pass filtering features slower than 20ms, together with  $dW_p/dt$  is plotted in Fig. (7h). During the burst,  $dW_p/dt$  drops to values around -1MW, which is a significant fraction (25%) of the  $\approx 0.3 \times 13\text{MW}$  input from the perpendicularly-injected NBI systems. However, as the burst duration of  $\sim 2\text{ms}$  is much shorter than the  $\sim 100\text{ms}$  slowing down time, the overall effect on fast ion losses is reduced. The drops are of order of 1kJ, which is  $\approx 0.1\%$  of the  $\sim 1\text{MJ}$  of total stored energy. From simulations, the total fast particle energy in these shots is comparable to the thermal energy. Therefore, each burst on its own is unlikely to cause enough energy loss to explain the lower  $T_i$  in the H-rich shots. However, if the burst events are not immediately redistributing the ions outside the plasma volume, the change in  $W_p$  may only be slight as it is a globally-averaged quantity. In order to understand clearly the evolution of the stored energy in the burst and recovery phases, another cross-correlation calculation is performed between the PCI phase velocity and the stored energy, plotted in Fig. (8e). This figure tends to give the average evolution

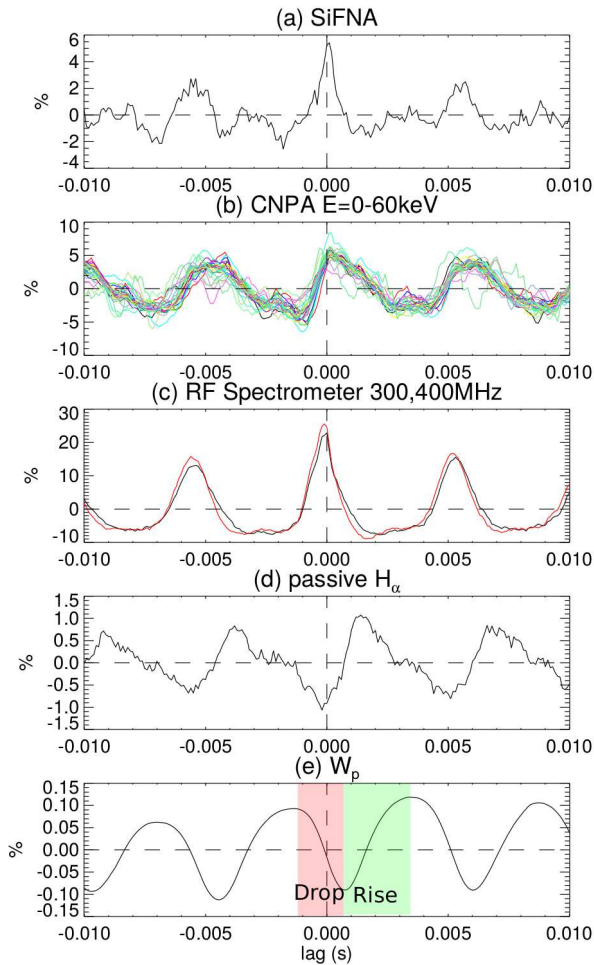


Figure 8. Cross-correlation measure using  $\gamma^{rel} \times 100\%$  between PCI phase velocity and (a) SiFNA, (b) CNPA energy channels (in different colours) up to 60keV (larger energies are dominated by noise), (c) the ICE RF spectrometer in the 300,400MHz channels, (d) passive  $H_\alpha$ , and (e) the diamagnetic stored energy  $W_p$ . Discharge #127708, 30% He.

of the stored energy in the recovery phase. This clarifies that there are only two phases: the drop in energy associated with the burst, then the rise in stored energy after the MHD event has finished. However, there is no significant period where the stored energy remains constant, indicating that the stored energy never completely “recovers” after each burst. Therefore, although each burst only loses  $\sim 1\text{kJ}$ , the combined effect of all these bursts may reduce the stored energy by more than that value. Analysis of  $W_p$  is not completely conclusive, as changes during each burst may also be associated with changes in the bulk ion and electron density and temperature profiles.

### E. Ion species dependence of bursts and estimation of loss current

The bursting-MHD features described are more frequent in more H rich discharges. Phase velocity

time traces at  $\rho = 0.75$  are compared between each of the four shots discussed in Sec. (II) in Fig. (9a1-4), together with low-pass filtered ( $f < 25\text{kHz}$ ) traces of the magnetic probe signals, to capture the EIC events in Fig. (9b1-4), and traces of the RF ICE spectrometer at 300 and 400MHz in Fig. (9c1-4). It is clear that in the He-rich discharge, the bursts only occur ever 20-30ms, whilst in the H-rich discharge, the bursts occur roughly every 4ms. This suggests that the fast particle population and fast particle beta, which drive the modes is substantially different in each of the four cases. Moreover, these changes are unlikely to be due to any changes in the bulk plasma properties, as the  $n_e$  &  $T_e$  profiles are near identical in all cases, and the  $T_i$  profile changes as shown in [11]. It was shown in that paper that the ion heating power per particle was also unchanged between these shots.

For all discharges, there are signatures of the losses in the RF ICE spectrometer in Fig. (9c1-4), however these vary considerably in shape and magnitude. This may reflect a change phase-space redistribution of fast ions relative to the sensitivity of the diagnostic. Also, the RF emission intensity may not necessarily be linearly proportional to the energetic particle losses. Bursts in the magnetic signals are always perfectly correlated those in the phase velocity, even amongst these four discharges. Furthermore, in He-rich discharges, the bursts in the magnetic probe signals are considerably stronger, whilst the change to the phase velocity is around the same value. The longer period between events in He suggests that the modes are more “stable”, however the magnetic probe signatures are larger, with the same resulting fast ion losses, assuming that they can be conveyed by the PCI velocity.

In all cases, the duration of the bursts is roughly constant at around 2ms. However, the magnitude of the bursts in phase velocity (i.e. the fast-ion driven radial electric field) are not always the same, more particularly for the 21.8% and 52.4% He shots. To quantify the details of the PCI phase velocity change in more detail, the relative burst rate is computed, defined by:

$$r = 1/T \int_{\Delta v_{phase} > v_{crit}} dt, \quad (8)$$

where  $v_{crit}$  is arbitrarily defined (here at  $-2\text{km/s}$ ) to distinguish these MHD events, and  $T$  is the time window length (here we use 0.1s). If we assume that bursts represent fast ion losses, then a quantity related to the average fast ion loss current can be evaluated the integral of the change in phase velocity:

$$j_{loss} = 1/T \int_{\Delta v_{phase} > v_{crit}} \Delta v_{phase} dt, \quad (9)$$

assuming that the losses are all dependent on the magnitude of the initial change in  $v_{phase}$  (during the first 0.1ms of the burst), and that the  $\sim 2\text{ms}$  timescale for the relaxation is the same in all cases. A

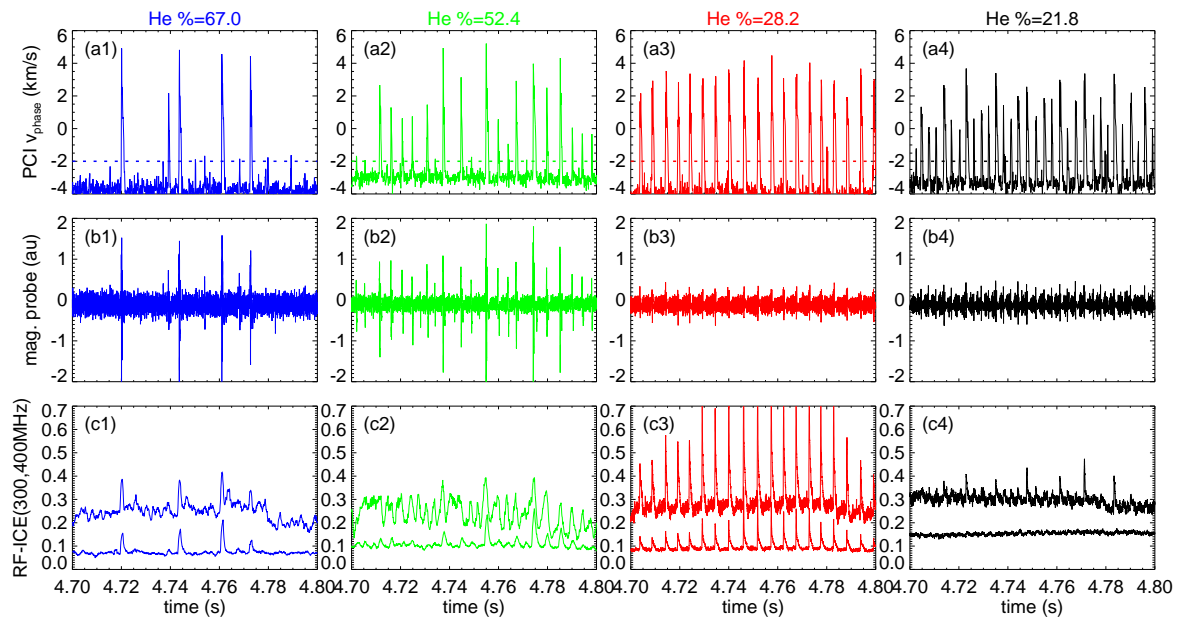


Figure 9. Comparison of the temporal evolution of (a) the phase velocity at  $\rho = 0.75$ , as well as (b) the low frequency component of filtered magnetic probe signals ( $<25\text{kHz}$ ), and (c) RF ion cyclotron emission spectrometer channels at 300,400MHz, showing how the bursting behaviour varies with He fraction (1-4). The critical velocity  $v_{crit}$  defining a burst is indicated with the dashed line in (a).

precise evaluation of the loss current, considering the physics of momentum transport and fast ion redistribution is beyond the scope here, but has been touched upon in [23].

The average change of phase velocity for each burst  $\Delta v_{avg}$  can be calculated from

$$\Delta v_{avg} = j_{loss}/r \quad (10)$$

The burst rate and  $\Delta v_{avg}$  are plotted vs. He concentration in Fig (10a,b), whilst the dependence of  $j_{loss}$  is discussed in Sec. (VD). It is clear that the burst rate is inversely related to the Helium concentration, however, the values of  $\Delta v_{avg}$  are lower for the 21% and 53% He concentration discharges. One possibility for this is the additional viscosity/damping to the rotation in the presence of magnetic perturbation, which can introduce higher harmonic field ripple [45]. To investigate the role of this perturbation, the amplitude of the magnetic probe signals, filtered between 25-50kHz (to obtain the component with 30kHz and associated chirping features associated with  $m=4, n=1$ ), averaged over times both with bursts and without bursts are shown in Fig (10c). It is clear the magnetic probe amplitudes in between bursts are higher for the 21% and 53% Helium discharges, which are precisely the ones with smaller  $\Delta v_{avg}$ . Also in this figure, it is observed that the amplitude of 25-50kHz fluctuations is higher during the bursts but with little dependence on the He concentration.

Finally, in Fig. (10d), the magnetic probe amplitude for low frequency components ( $f < 25\text{kHz}$ ) is indicated, which tend to encapsulate the EIC-like burst features ( $m \sim 0 - 1, n = 1$ ), both during and between bursts. It is clear that the EIC mode amp-

litude increases markedly with He concentration, being near the inter-burst level for H rich discharges, and increasing to a level 5 times the value in between bursts in He rich discharges. This behaviour is somewhat “anti-correlated” with the burst rate dependence indicated in Fig. (10a). This is invaluable information to understand the drive of the EIC: in He discharges, the mode is more “stable”, in that the modes are driven less frequently, however when an event occurs, it is larger. However, the fast ion losses for each event, characterised by  $\Delta v_{avg}$ , are largely unchanged (excepting for the small reduction in the 21% and 53% discharges as discussed).

#### F. Turbulence and heat transport modulation due to bursts

During the burst events, as has been shown, the velocity reverses, producing strong  $E \times B$  velocity shear. Associated with this, the density fluctuations decrease dramatically for that period of time. In [23], it was shown that strong EIC events were associated with a transient improvement of particle and both electron and ion thermal confinement, and this is certainly the case for electron thermal confinement in these discharges, as shown below. On the other hand, the average level of turbulence hardly changes between H and He discharges [9], despite the improvements during the bursts in H. This complex interplay therefore requires more detailed analysis. Whilst it would be informative to understand the correlation with ion temperature, the SNR of the CXRS data is not sufficient to make any conclusion. On the other hand, the ECE system shows clear changes in the electron temperature which can

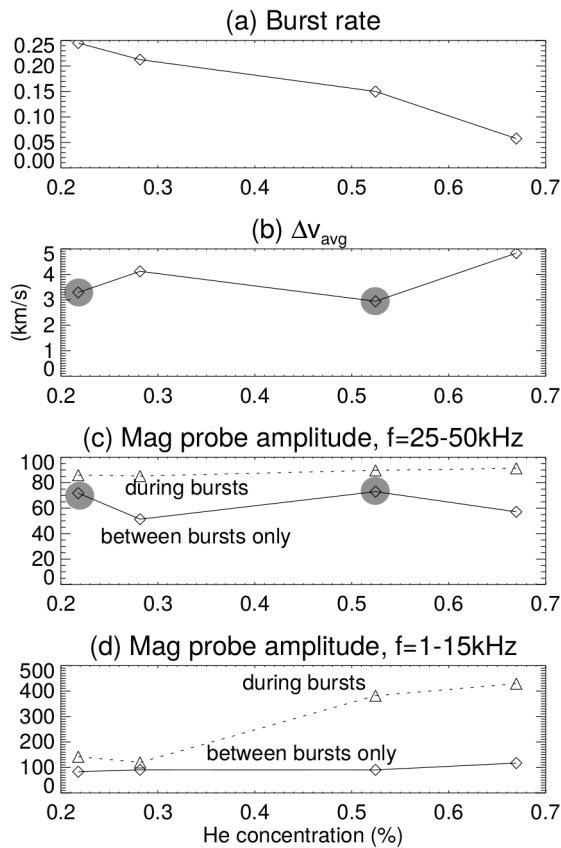


Figure 10. (a) The burst rate (defined as the fraction of time for which  $v > v_{crit}$ , evaluated over 4.5-5s, calculated from the time history of the phase velocity at  $\rho = -0.75$  as shown in Fig. (9)) plotted as a function of He concentration. (b) The average velocity of each burst,  $\Delta v_{avg}$ , calculated as a function of the He concentration. Average amplitude of the magnetic probe signals for 25-50kHz (c) and 1-15kHz (d), as a function of the He concentration, analyzed during time windows during bursts, and in between bursts. The points in grey highlight the correlation between  $\Delta v_{avg}$  and high frequency mode amplitude between bursts.

be analyzed.

The electron temperature, measured using electron cyclotron emission (ECE) diagnostic, shows distinctive changes during the burst events. To clarify this, the normalised correlation function  $\gamma^{chg}$  is calculated in Eq. (2), indicating on average, the change in value of temperature with each burst. This is indicated in as a 2D plot as a function of delay time and normalised radius in Fig. (11a) for the 30% H rich discharge. There are clear temperature changes associated with the bursts, including a temperature drop around -20eV associated with the burst (at  $\rho = 0.9$ ,  $t_{lag} = 0$ ), and a maximum temperature rise around  $\sim 30$ eV at  $\rho = 0.8$ ,  $t_{lag} = 1$ ms. The increase in the temperature is suggestive of a transport improvement, possibly generated by the increased velocity shear. According to Fig (4a) the change in  $E \times B$  rotation is largest around change around  $\rho = 0.8$ . so that the region  $\rho = 0.6 - 0.8$  is

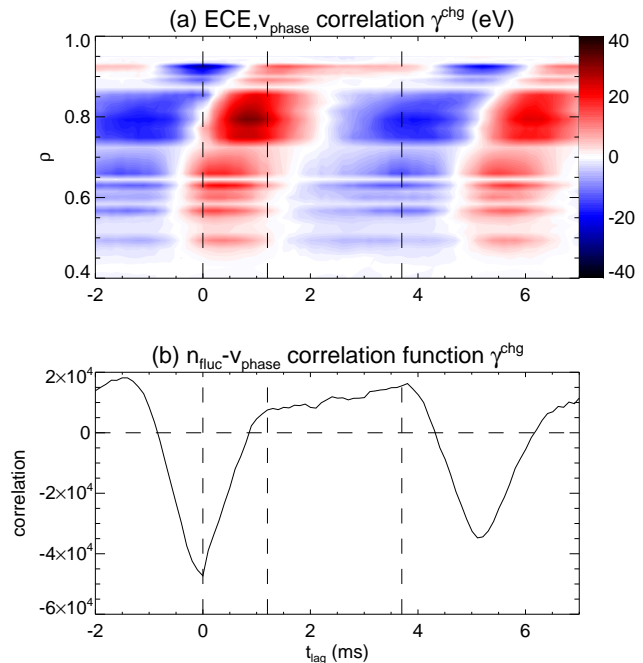


Figure 11. Normalized correlation  $\gamma^{chg}$  (from eq. (2)) between  $v_{phase}$  and (a) ECE signals as a function of  $\rho$  and delay time  $t_{lag}$ , and (b)  $\tilde{n}$ , for 30% H shot #128708.

where the strongest velocity shear is situated. This corresponds well with the region of largest temperature increase after the event. After the bursting event has ceased, the temperature decreases, and this excess heat tends to propagate outwards to  $\rho = 0.9$  at  $t_{lag} = 1 - 3$ ms as shown in Fig. (11a). Thus, the apparent temperature “drop” at  $t_{lag} = 0$  is more a consequence of the delayed propagation of the heat pulse from further in.

The cross-correlation  $\gamma^{chg}$  between the phase velocity and the fluctuation level (both at  $\rho = 0.75$ ) is plotted for the 30% discharge in Fig. (11b). It is clear that the drop in fluctuation amplitude, between  $t_{lag} = -1$  to 1ms is well correlated with the  $T_e$  rise at  $\rho = 0.8$ , and the “flat top” increase in fluctuation-amplitude is correlated with decreasing electron temperature at  $\rho = 0.8$ . While the average central electron temperature does not change with He concentration, there is in fact some transient change with each burst, but it is more concentrated towards the edge. It is worthwhile to keep in mind that for these discharges, it was shown that the turbulence the amplitude is well correlated with ion temperature gradient [9], consistent with it being in the ITG regime. We also note that it was shown that for EICs [23], both ion and electron thermal conductivity was improved after each burst, purely showing that the two are connected, presumably as both are affected by  $E \times B$  shear.

The average turbulence level is the same in the H and He-rich discharges [9], and, because of the larger occurrence of bursts in H-rich discharges, where



the fluctuations are suppressed, the fluctuation-level in-between bursts is in-fact higher. Comparing the electron temperature in Fig. (11a), and turbulence amplitude in figure (11b), the turbulence amplitude increases up to a delay of 4ms after the burst event, when the “heat pulse” has propagated towards the edge, thereby increasing the electron temperature gradient (at some location) and thus the “potential” drive for the turbulence (strictly, the ion temperature gradient is expected to have the most dominant influence). However, it is expected that a similar improvement may occur to the ion temperature, as this was reported for an EIC event in [23]. The details of these bursts allows to understand the critical gradient behaviour of turbulence as predicted by gyro-kinetics [12].

#### IV. VARIATION OF CONFINED FAST ION DENSITY

The time-averaged value of various measures of the fast-ion distribution function may give further clues as to the reason for the ion temperature dependence on He concentration. This may resolve the issue of understanding the magnitude of the fast ion losses from the MHD events, or may indicate how other processes, such as neutral penetration into the plasma volume, and charge-exchange losses, play a role.

##### A. Compact Neutral particle analyser

The NPA systems which were utilised in Sec. (IIID) including the CNPA and the SiFNA can convey information also about the average level of fast ions in the He/H comparison discharges. The complicating factor, however, is that the effect of the difference of the cross-sections between fast hydrogen ions and background hydrogen or background Helium atoms has to be considered, as well as the variation in the background neutral density. Whilst this may seem complicated, a simple analysis of the energy-resolved CNPA system can give a clue as to the variation on the fast ion density in between the H and He-rich discharges.

The CNPA energy spectrum for the H and He rich shots is plotted in Fig. (12). For energies lower than 50keV, the He-rich discharges have lower signal, whilst for  $E > 50\text{keV}$ , H-rich discharge has more NPA signal. The charge-exchange cross-sections for H and He collisions with H ions has been obtained from ADAS [46]. The H-He cross-section is lower for  $E < 40\text{keV}$ , and higher for  $E > 40\text{keV}$ . The fast ion density  $n_{fast,H}(E)$  as a function of energy  $E$  can be related to the NPA signal  $S_{NPA}(E)$  from the equation:

$$n_{fast,H}(E) \propto \frac{S_{NPA}(E)}{\sigma_{H-H^+}(E)n_{H^0} + \sigma_{He-H^+}(E)n_{He^0}} \quad (11)$$

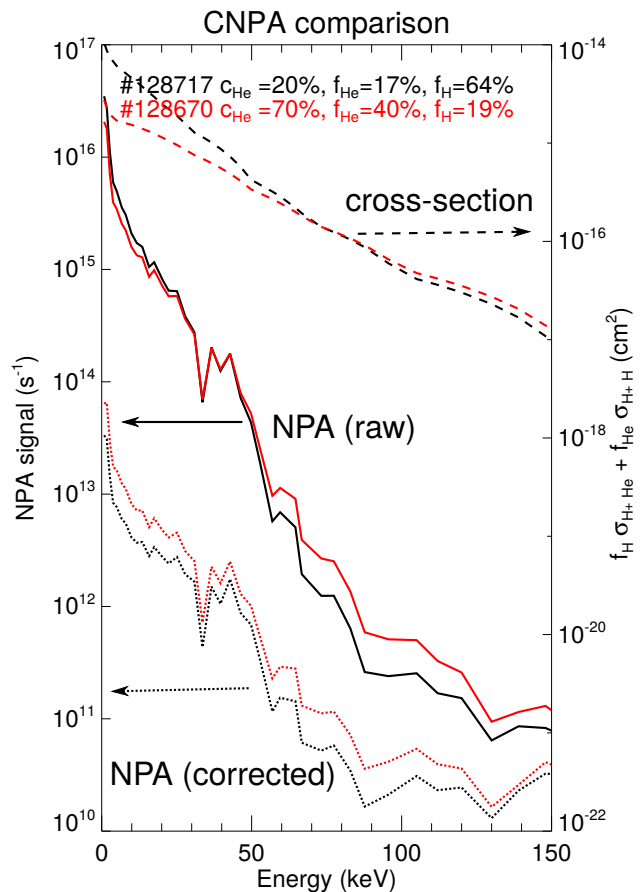


Figure 12. Solid line: CNPA Energy spectra for the interval 4.7-4.9s for the He and H rich discharges (red,black). Dashed line: species-weighted charge-exchange cross-section  $\sigma_{H-H^+}(E)f_H + \sigma_{He-H^+}(E)f_{He}$  (numbers on the right-hand axis). Dash-dot line: CNPA signal corrected with this cross-section factor.

where  $\sigma_{H-H^+}$ ,  $\sigma_{He-H^+}$  are the energy dependent charge-exchange cross-sections,  $n_{H^0}$ ,  $n_{He^0}$  are the background neutral density of Hydrogen and Helium (at the position of charge-exchange). Whilst strictly, the radial dependence of all these quantities is necessary for a thorough analysis, the known cross-section-dependent effects can be divided out in proportion to the known fraction of Helium and Hydrogen ion densities  $f_{He}$ ,  $f_H$ , as defined in Eq. (4,5), which should be proportional to the neutral densities at the periphery of the plasma. (In fact, the neutral spectral lines are used to monitor the plasma ion density). This factor, and the corrected CNPA spectra are indicated in Fig. (12). After normalisation, He-rich discharges have more signal than H-rich discharges. On the other hand, as discussed earlier in Sec. (VA), the donor neutral density profile decreases much more rapidly into the plasma for He discharges, and so this result suggests that there is in-fact a higher fast ion density at some radius near the edge of the plasma (where most of the NPA signal comes from) in He discharges.

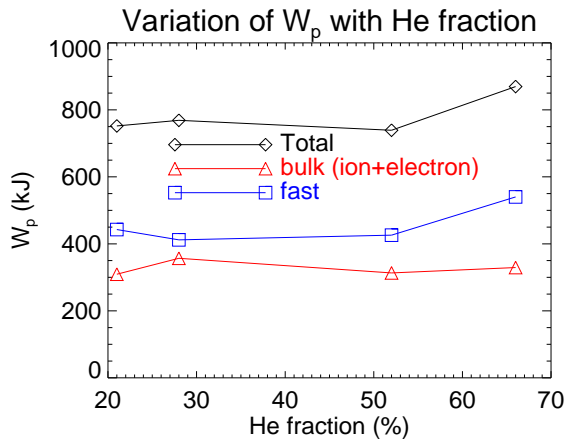


Figure 13. Variation of diamagnetic  $W_p$ , thermal  $W_p$  and inferred fast ion component with He fraction discharge for the interval 4.5-4.9s. Uncertainties of around 5% in the thermal and therefore fast ion stored energy due to uncertainties in the Thomson and charge exchange data, and uncertainty of the flux surface mapping.

### B. Diamagnetic stored energy

The diamagnetic loop signal varies in between the H and He rich discharges. To infer the fast ion component, the stored energy in the bulk plasma must be evaluated and subtracted out. For this, the Thomson scattering system is used to determine electron density and temperature, whilst the CXRS system is used for the ion temperature, and the ion density is accounted for according to the uniform ratio evaluated from passive spectroscopy. These results are plotted in Fig. (13). As the diamagnetic loop is sensitive only to the perpendicular energy, the fast ion energy represents the perpendicularly-injected beams. It is clear that the fast-ion component of the signal increases with He concentration just like the NPA signal, except for the discharge at 30% He concentration.

## V. PHYSICS DISCUSSION

### A. Effect of ion species on background neutral density

A change of working gas from H to He can produce can significantly impact the background neutral density in the plasma region. This can be understood by considering a simple model for neutral penetration in plasma, which is developed for H plasmas [47]. In this model, a two fluid type 'quasi-kinetic' model is employed to characterize the penetration of neutrals into the plasma from the edge, separated into "slow" neutrals, having a velocity characteristic of the background edge neutral temperature, and "fast" neutrals, which have undergone a charge-exchange reaction. The e-folding lengths for penetration are given by slow decay length  $L_s = v_{tn}/n_i \sqrt{(\xi_{iz} + \xi_{ins})(2\xi_{iz} + \xi_{ins})}$ , and

fast decay length  $L_f = v_{ti}/n_i \sqrt{\xi_{iz}(2\xi_{iz} + \xi_{inf})}$ , where  $v_{tn}$ ,  $v_{ti}$  is the neutral and ion thermal velocities, and  $\xi_{iz}$  is the electron impact rate coefficient, and  $\xi_{ins}$ ,  $\xi_{inf}$  is the rate coefficient for charge exchange between ion and neutral species for the slow and fast populations respectively. Whilst this model is simple and neglects complex kinetic and geometrical issues associated with the boundary plasma, it serves to illustrate the physics. For the typical parameters of the edge plasma, taken for example with  $T_e = T_i = 100\text{eV}$ ,  $T_n = 1\text{eV}$ , and  $n_e = 10^{18}\text{m}^{-3}$ , rising to  $10^{19}\text{m}^{-3}$  within 12cm [11], and obtaining the relevant cross-sections for ionization and charge exchange from [48], one deduces  $L_s = 27\text{cm}$  (for  $n_e = 10^{18}\text{m}^{-3}$ ) and  $L_s = 2.7\text{cm}$  (for  $10^{19}\text{m}^{-3}$ ), so it might penetrate realistically to a depth  $\approx \sqrt{2.7 \times 12\text{cm}} = 6\text{cm}$ . For fast neutrals, a higher density of  $10^{19}\text{m}^{-3}$  is appropriate and so  $L_f = 30\text{cm}$ . The relative abundance of fast neutrals depends on the ion density at the point of charge exchange, which can occur most appreciably only in the last 6cm of plasma, where the density and temperature can climb to appreciable values.

For Helium plasma, the difference is that the charge-exchange reaction which can result in fast neutrals can only occur for singly-charged Helium ions:  $\text{He} + \text{He}^+ \rightarrow \text{He}^+ + \text{He}$ . For the reaction  $\text{He} + \text{He}^{2+} \rightarrow \text{He}^+ + \text{He}^+$ , there are no neutral reaction products. Considering that the ionization potential for  $\text{He}^{2+}$  is 54eV, the abundance of  $\text{He}^+$  would decrease dramatically as the electron temperature increases which would certainly be very far out from the core region. Therefore, charge exchange and the production of fast neutrals could only occur within the last few mm of plasma, where the ion density and temperature are much lower (compared with Hydrogen). Consequently, the neutral density in the core of Helium-rich plasma is expected to be lower than in Hydrogen rich plasma.

Additionally, since these are matched electron density discharges, the neutral density in He need only be half of that of H on account of having two bound electrons. We also note in these discharges are neither completely pure H or pure He, the penetration of H into the mixed He/H discharges may contribute a significant effect.

A detailed calculation of the neutral profiles has not been undertaken for these discharges. However, it is expected that the results published in [49] can be used to understand its effect. In that work, the relative values of the ionization rate calculated with the EIRENE code [50], were compared between density and power-"matched" H and He rich discharges, very similar to the discharges studied in this paper, however they were heated only by ECH. This result is reproduced in Fig. (14). As the density and temperature was almost identical, and given that the electron-impact ionization rate coefficient for H is very similar to that for He [48], the difference is mostly due to the neutral density. It is clear that the He neutral density is almost an order of magnitude smaller in He discharges compared to H discharges, and the discrepancy appears even out towards the



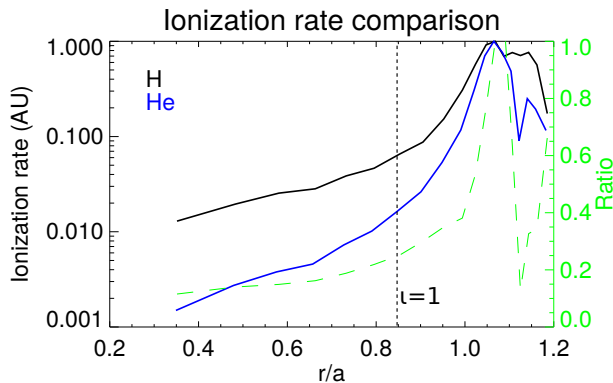


Figure 14. Comparison of the ionization rate profile between H rich shot #118352 and He rich shot #119049 (which were ECH heated only).

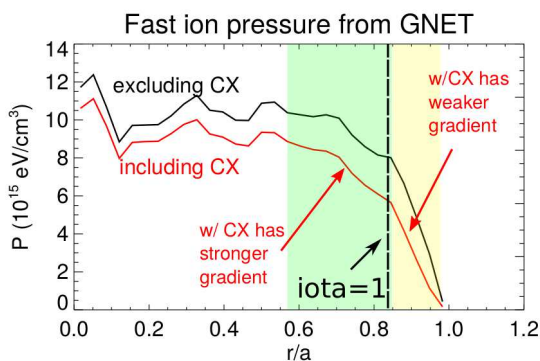


Figure 15. Calculation using the GNET code of the fast ion pressure profile per MW for perpendicular beam injection comparing the effects with and without charge-exchange losses in the ion-ITB H rich shot #128717.

edge as far as  $\rho = 0.9$ . An additional piece of evidence that the Helium neutral density is lower in the core arises from the thermal broadening of the neutral spectral lines. It was shown [51] that the radial distribution of Helium could be obtained from the broad wings of the neutral Hydrogen spectral lines, in combination with data about the electron temperature profile. However, observations show much narrower wings of the Helium spectral lines indicating less charge exchange component – i.e. lower Helium density in the core regions.

### B. Influence of background-neutral charge-exchange on fast ion pressure

The neutral density profile can have a significant impact on charge-exchange losses of  $H^+$  ions from the neutral beams. The fast ion pressure for the perpendicularly-injected beams, calculated using the GNET code [33], is plotted in Fig. (15), for the H-rich discharge #128717, both including (red) and excluding (black) CX losses. The total stored energy from these beams decreases by about 20% because of charge-exchange. Surprisingly, charge-exchange tends to decrease the fast ion pressure in

the core despite the fact that there are less neutrals there. This may be because the low-energy neutral beams (33-43keV) tend to ionize close to the edge of the plasma, where the background neutral density is high and thus they are susceptible to charge exchange loss. The fast ions in the core of the plasma may arise due to diffusion from the source region near the edge.

As the GNET code does not presently model the background Helium neutral distribution, nor the charge-exchange process with Helium, it is not possible to clearly model the difference of the fast ion pressure between H and He rich discharges. However, given that the background neutral density is lower in Helium, the fast ion pressure will be higher. Another contributing factor is that the charge-exchange cross-section  $\sigma_{H+He}$  is lower than  $\sigma_{H+H}$  in the range 0-60keV as shown by the dashed lines in Fig. (12), contributing to lower CX losses. This will impact on the power delivered to ions from the perpendicularly-injected beams and to our knowledge has not been included in the power balance analysis presented in [9, 11].

### C. Drive and damping of fast particle MHD in He and H discharges

The fast-ion pressure gradient should be the main drive term to determine the instability threshold of fast ion MHD events. To explain the higher rate of EIC events in H-rich discharges, the fast-ion pressure gradient should be greater at the position  $\rho = 0.83$ , where the mode is resonant with the  $\iota = 1$  surface. From Fig. (15), the gradient in fast ion pressure is slightly larger in the region  $\rho = 0.6 - 0.85$  with charge-exchange present, i.e. more like the H-rich case than the He-rich case. But, there is in-fact a decreased pressure gradient region in the peripheral region, i.e.  $\rho > 0.85$ , as indicated by the shading in the figure. Thus it is difficult to make a clear conclusion from this analysis. A full simulation of the fast ion pressure distribution in the presence of Helium background plasma, might further alter the spatial gradient beyond the “excluding-CX” case: for example, as charge-exchange losses are still prevalent at the edge of Helium discharges, they might tend to enhance the edge fast-ion pressure gradient. Further modelling is required to solidify this argument.

Mode damping may play a role in the apparent change of mode stability going from H to He. Possible mechanisms include continuum damping, mode coupling, electron collisional damping and Landau damping on ions and electrons. Of all these mechanisms, we draw attention to ones which would exhibit a change in behaviour going from H to He. The obvious candidate is Landau damping on the ion distribution function.

For Landau damping, resonance with bulk plasma ions with the mode has a stabilising effect, depending on the velocity gradient of the ion distribution function  $df/dv$  according to the terms in the Vlasov equation. Landau damping is often determined by a

resonance between the mode and particular particles in the bulk distribution function, where the magnitude of the interaction is determined by the ratio of the phase velocity to the thermal velocity. For high frequency fast ion instabilities like TAEs, this is often considered negligible, because the mode velocity is much faster than the ion thermal velocity. However, for the modes present here their low frequency means that the phase velocity is much lower, so it is worthwhile considering that Landau damping could play a role. For both the EIC mode at 8kHz with  $m=1, n=1$  and the mode at 30kHz with  $m=4, n=1$  the phase velocity (in the helical direction of propagation) is  $v_{phase} \sim 28\text{km/s}$ . This is considerably smaller than  $v_{th}$ , which for H discharges at 1keV (near the  $\iota = 1$  surface) is  $\sim 400\text{km/s}$  and  $\sim 200\text{km/s}$  for He.

A precise evaluation of the role of Landau damping requires a model for the specific type of MHD mode. One mode of interest to consider is the ion acoustic oscillation [52], which has a dispersion relation given by  $\omega/k = (1.45 - 0.6i)v_{th}$ , where the negative imaginary component represents Landau damping. Whilst the modes of interest have much lower phase velocity than the thermal velocity, they are in the acoustic range and demonstrate that Landau damping could occur in this frequency range. Changing from He to H, the thermal velocity changes a factor of 2 as it scales as  $v_{th} \sim 1/\sqrt{A}$ . If we consider the  $v_{th}$  and charge ( $Z$ , controlling ion density scaling for constant electron density) dependence of the ion distribution function, i.e.  $f(v) \sim Z^{-1}v_{th}^{-1} \exp(-v^2/v_{th}^2)$ , we can estimate simply how the velocity space gradient  $\partial f(v)/\partial v$  at  $v = v_{phase} = 28\text{km/s}$  changes from H to He. This gradient is  $\approx 4$  times larger in He than H, and so will contribute to greater Landau damping in Helium.

On the other hand, we note another damping effect: the stabilisation of the EIC that can occur with ECH which increases temperature and thus decreases the magnetic Reynolds number, which has the effect of reducing the radial width of the interchange mode eigenfunction [53]. In this case, moving from H to He would have the effect of reducing the magnetic Reynolds number, enlargening the eigenfunction, so would not be the mechanism behind the stabilization.

#### D. Role of EIC events on ion heating

The key results from this paper are summarized in Fig. (16), including the He concentration dependence of (a) central ion temperature, (b) the integral of the corrected NPA signal over energy, (c) the fast ion  $W_p$  component obtained from Sec. (IV B) and (d) a rough estimate of the fast ion loss current  $j_r$  from the EIC events, obtained from PCI data, computed using Eq. (9). For increasing He concentration, the ion temperature increases and the EIC burst rate goes down. Measures of confined fast ion density increase.

From this correlation we can speculate whether

the decreasing burst rate / fast ion losses in He might be a cause for increasing ion temperature. Whilst the improvement of transport is definitely expected from the gyro-Bohm scaling, we note from Sec (II) that the improvement was not enough to fully explain the temperature increase particularly near the edge of the plasma. The increase in the fast ion energy content in Fig. (16b,c) in He discharges might further explain the strong ion temperature dependence. In particular, it was shown that the edge pedestal value of ion temperature increased with He concentration [9]. This increase may be due to a reduction of fast ion losses, or an increase in the direct charge-exchange losses of perpendicularly injected fast ions to background neutrals, which are more abundant in Hydrogen, or a combination of both.

The 2D PCI diagnostic clearly revealed bursting events where the phase velocity reversed to the electron diamagnetic direction in the region  $\rho = 0.6 - 0.9$ , and is attributed to the change of electric field associated with fast ion losses on the basis with correlation with fast ion diagnostics in Sec. (III D) including a lost ion RF spectrometer, the compact NPA system, as well as the diamagnetic loop signal. It is difficult to assess the magnitude of losses arising from the fast-ion MHD with present diagnostics. On one hand, the changes in the diamagnetic stored energy with each burst are only around 1kJ out of a total of 1MJ, which would suggest that the losses are not significant. However, the redistribution of fast ions may mask any local change of the fast ion pressure. Furthermore, it is not clear, from the correlation analysis in Fig. (8e), that the stored energy is saturating in-between burst events, suggesting that the  $\Delta W_p$  value for each burst is not indicative of the net effect for a series of MHD events.

## VI. CONCLUSIONS

*Observation of fast ion MHD:* This activity consists of EICs at around 8kHz with  $m/n=1/1$  and an unidentified mode at 30kHz with  $m/n=4/1$ . These EIC bursts consist of marked changes in the radial electric field, which is derived from the phase velocity of turbulence measured with the 2D phase contrast imaging (PCI) system. Similar bursts are detected in edge fast ion diagnostics including CNPA, SiFNA and ICE RF spectrometer channels at 300,400MHz. These EIC burst events appear to be similar in character though weaker than those reported in [23].

*Stability of EIC affected by ion species:* The change of the nature of the bursts with He concentration may help to understand the destabilisation mechanism of EIC bursts. Change of drive and damping mechanisms related to the change of mass and charge of Helium may be playing a role, including change of the fast ion pressure gradient near the 1/1 rational surface, and damping of the mode on the bulk ion distribution function. In Helium, there is a longer time between events as shown by Fig. (10a),

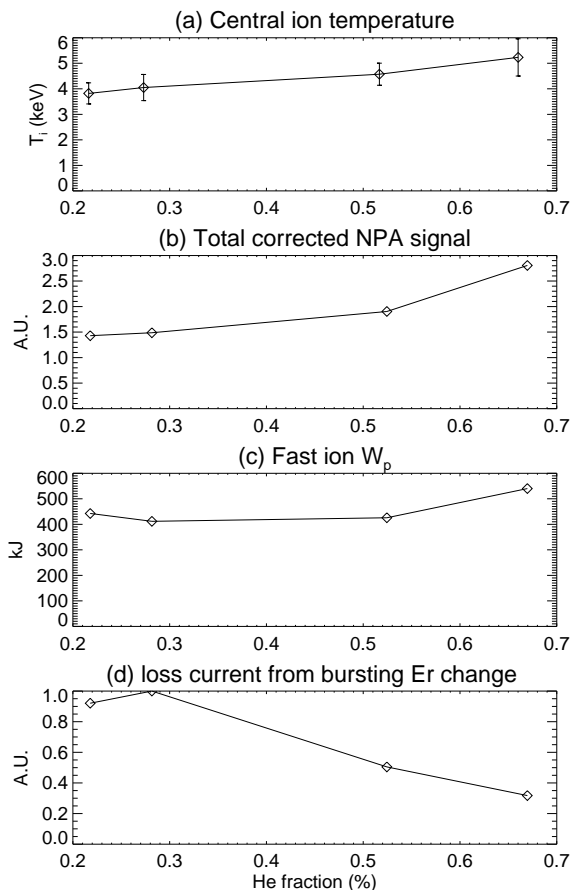


Figure 16. Comparison of the He fraction dependence of: (a) Central ion temperature averaged over  $\rho < 0.3$ , (b) Integral of the corrected NPA signal over energy, (c) Fast ion  $W_p$  value obtained from analysis of the diamagnetic loop and bulk contribution and (d) fast ion losses calculated from PCI phase velocity using Eq. (9).

and EIC amplitude is larger as shown in Fig. (10d). However, they result in very similar fast particle losses characterized by the change in electric field indicated in Fig. (10b). This behaviour is similar to that recently shown by Deuterium discharges [54].

*Effect of EIC-induced fast-ion losses on ion heating power:* Whilst the fast ion diagnostics are not quantitative enough to clarify the magnitude of the fast-ion losses from each event, the observed correlation of the fast ion loss current with the confined fast-ions and the ion temperature suggests that there may be a significant amount of power lost from each EIC event. This was suggested in the original article on the EIC [23].

*Turbulence suppression:* Fluctuation amplitude is suppressed during the EIC bursts. Although the average turbulence level stays independent of Helium fraction, there is lower edge turbulence in the phases of the MHD bursts, which are more prevalent in H-rich discharges. However, this is offset by a larger level of turbulence in the period between these bursts, most particularly in H rich discharges. Thus, the result is consistent with gyro-Bohm scaling.

The implication of this work is that fast ion in-

stabilities must be considered in any transport, or turbulence study, just as with bulk plasma instabilities. Energy lost from fast ion instabilities may degrade the heating power and thus affect any energy transport analysis carried out, and the changes in the radial electric field, time averaged, can considerably change the transport properties. Also, change in working gas can dramatically affect fast ion instabilities, either through change of drive, or through Landau damping on bulk ions. This is analogous, but different to the stabilization of the EIC that can occur due to the Magnetic Reynolds number changing at higher temperature [53].

Now that the first LHD Deuterium campaign has concluded these results will complement the understanding of a comparison of EIC events between Hydrogen and Deuterium (D) plasma. Bursts in D plasmas with D perpendicular beams are larger and less frequent than those of H beams into an H plasma. This is similar to the results reported in this paper where H beams injected into He plasma are larger and less frequent than Hydrogen plasma. Furthermore, the EIC bursts in D plasma can induce a significant loss of neutron yield [54], with a long time to recover between events, suggesting that the EIC can cause a large loss of heating power.

Further analysis is required to understand the drive of the 30kHz mode observed and to connect that to the fast ion instabilities. Since this mode bursts in amplitude with the EIC events, and has the same poloidal propagation velocity it suggests that it may be a coupling with the EIC event and/or with the precession of trapped fast ions from perpendicular beam injection. It is also a mystery of why the 8kHz EIC and the 30kHz mode propagate in the electron diamagnetic direction despite the deeply trapped beam ions propagating in the ion diamagnetic direction. Improvements in modelling of fast ions and background neutrals to include bulk Helium in the AURORA and GNET codes would enable understanding of the mode suppression in Helium. Finally, the hypothesis of the role of Landau damping in on the EIC would be solidified with a more detailed analysis of the wave/particle interaction.

## ACKNOWLEDGEMENTS

C. Michael gratefully acknowledges the support of the NIFS directorate for the invitation as a visiting associate professor for the months of June-July 2016. He also acknowledges gratefully colleagues at NIFS for being responsive to providing data and interpretation. We would like to acknowledge K. Toi, Professor Emeritus of NIFS and X. Du of UC Irvine for invaluable discussions about this topic. Work on this paper was also funded by the Australian Government's National Collaborative Research Infrastructure Strategy (NCRIS), NIFS grants NIFSULHH013, NIFS10ULRR702, NIFSULHH004, NIFSULHH005, NIFSULHH02, NIFSULHH028, NIFS16KLER045, NIFS14UNTT006 and JSPS kakenhi grant number 16H04620p.

- 
- [1] H. Urano, T. Takizuka, T. Fujita, Y. Kamada, T. Nakano, N. Oyama and J. T. T. the, *Nuclear Fusion* **52** (2012) (11), p. 114021
- [2] R. Lorenzini, M. Agostini, F. Auremma, L. Carraro, G. D. Masi, A. Fassina, P. Franz, M. Gobbin, P. Innocente, M. E. Puiatti, P. Scarin, B. Zaniol and M. Zuin, *Nuclear Fusion* **55** (2015) (4), p. 043012
- [3] M. Bessenrodt-Weberpals, F. Wagner, O. Gehre, L. Giannone, J. V. Hofmann, A. Kallenbach, K. McCormick, V. Mertens, H. D. Murmann, F. Ryter, B. D. Scott, G. Siller, F. X. Soldner, A. Stabler, K. H. Steuer, U. Stroth, N. Tsois, H. Verbeek and H. Zoehm, *Nuclear Fusion* **33** (1993) (8), p. 1205
- [4] A. D. Gurchenko, E. Z. Gusakov, P. Niskala, A. B. Altukhov, L. A. Esipov, T. P. Kiviniemi, T. Korpilo, D. V. Kouprienko, S. I. Lashkul, S. Leerink, A. A. Perevalov and M. A. Irzak, *Plasma Physics and Controlled Fusion* **58** (2016) (4), p. 044002
- [5] U. Stroth, B. Brañas, T. Estrada, L. Giannone, H. J. Hartfuss, M. Hirsch, M. Kick, G. Kühner, S. Sattler, J. Baldzuhn, R. Brakel, V. Erckmann, R. Jänicke, H. Ringler, F. Wagner, E. G. the and W. A. S. T. the, *Physica Scripta* **51** (1995) (5), p. 655
- [6] H. Yamada, K. Ida, S. Murakami, K. Y. Watanabe, E. Ascasibar, R. Brakel, A. Dinklage, J. H. Harris, S. Okamura, F. Sano, U. Stroth, S. Inagaki, K. Tanaka, M. Goto, K. Nishimura, K. Narihara, S. Morita, S. Sakakibara, B. J. Peterson, R. Sakamoto, J. Miyazawa, T. Morisaki, M. Osakabe, K. Toi, N. Tamura, K. Ikeda, K. Yamazaki, K. Kawahata, O. Kaneko, N. Ohyabu, A. Komori and O. Motojima, *Fusion Science and Technology* **46** (2004) (1), pp. 82–90
- [7] K. Tanaka, S. Okamura, T. Minami, K. Ida, D. R. Mikkelsen, M. Osakabe, Y. Yoshimura, M. Isobe, S. Morita and K. Matsuoka, *Plasma Physics and Controlled Fusion* **58** (2016) (5), p. 055011
- [8] Y. Ohtani, K. Tanaka, T. Minami, S. Ohshima, K. Nagasaki, T. Akiyama, Y. Nakamura, H. Okada, S. Kado, S. Kobayashi, S. Yamamoto, N. Kenmochi, X. Lu, S. Konoshima and T. Mizuuchi, *Journal of the Physical Society of Japan* **86** (2017) (6), p. 064501
- [9] K. Tanaka, K. Nagaoka, S. Murakami, H. Takahashi, M. Osakabe, M. Yokoyama, R. Seki, C. A. Michael, H. Yamaguchi, C. Suzuki, A. Shimizu, T. Tokuzawa, M. Yoshinuma, T. Akiyama, K. Ida, I. Yamada, R. Yasuhara, H. Funaba, T. Kobayashi, H. Yamada, X. D. Du, L. N. Vyacheslavov, D. R. Mikkelsen, G. S. Yun and L. H. D. E. G. the, *Nuclear Fusion* **57** (2017) (11), p. 116005
- [10] K. Nagaoka, H. Takahashi, S. Murakami, H. Nakano, Y. Takeiri, H. Tsuchiya, M. Osakabe, K. Ida, M. Yokoyama, M. Yoshinuma, S. Morita, M. Goto, T. Oishi, N. Pablant, K. Fujii, K. Tanaka, N. Tamura, Y. Nakamura, X. Du, T. Ido, A. Shimizu, S. Kubo, H. Igami, R. Seki, C. Suzuki, Y. Suzuki, K. Tsumori, K. Ikeda, M. Kisaki, Y. Yoshimura, T. Shimojima, T. Seki, K. Saito, H. Kasahara, S. Kamio, T. Mutoh, O. Kaneko, H. Yamada and A. Komori, *Nuclear Fusion* **55** (2015) (11), p. 113020
- [11] K. Nagaoka, H. Takahashi, K. Tanaka, M. Osakabe, S. Murakami, S. Maeta, M. Yokoyama, K. Fujii, H. Nakano, H. Yamada, Y. Takeiri, K. Ida, M. Yoshinuma and L. H. D. E. G. the, *Plasma and Fusion Research* **11** (2016), pp. 2402106–2402106
- [12] M. Nunami, M. Nakata, H. Sugama, K. Tanaka and S. Toda, *Plasma Physics and Controlled Fusion* **59** (2017) (4), p. 044013
- [13] K. Tanaka, C. A. Michael, L. N. Vyacheslavov, A. L. Sanin, K. Kawahata, T. Akiyama, T. Tokuzawa and S. Okajima, *Review of Scientific Instruments* **79** (2008) (10), p. 10E702
- [14] W. W. Heidbrink, *Physics of Plasmas* **15** (2008) (5), p. 055501
- [15] J. A. Snipes, A. Fasoli, P. Bonoli, S. Migliuolo, M. Porkolab, J. E. Rice, Y. Takase and S. M. Wolfe, *Plasma Physics and Controlled Fusion* **42** (2000) (4), p. 381
- [16] W. Chen, X. T. Ding, Q. W. Yang, Y. Liu, X. Q. Ji, Y. P. Zhang, J. Zhou, G. L. Yuan, H. J. Sun, W. Li, Y. Zhou, Y. Huang, J. Q. Dong, B. B. Feng, X. M. Song, Z. B. Shi, Z. T. Liu, X. Y. Song, L. C. Li, X. R. Duan and Y. Liu, *Physical Review Letters* **105** (2010) (18), p. 185004
- [17] W. Chen, X. T. Ding, L. Yi, Q. W. Yang, X. Q. Ji, M. Isobe, G. L. Yuan, Y. P. Zhang, Y. Zhou, X. Y. Song, Y. B. Dong, W. Li, J. Zhou, G. J. Lei, J. Y. Cao, W. Deng, X. M. Song, X. R. Duan and H.-A. Team, *Nuclear Fusion* **50** (2010) (8), p. 084008
- [18] T. Hauff, M. J. Poeschel, T. Dannert and F. Jenko, *Physical Review Letters* **102** (2009) (7), p. 075004
- [19] A. R. Field, C. Michael, R. J. Akers, J. Candy, G. Colyer, W. Guttenfelder, Y. c. Ghim, C. M. Roach, S. Saarelma and M. T. the, *Nuclear Fusion* **51** (2011) (6), p. 063006
- [20] K. Toi, K. Ogawa, M. Isobe, M. Osakabe, D. A. Spong and Y. Todo, *Plasma Physics and Controlled Fusion* **53** (2011) (2), p. 024008
- [21] K. Toi, M. Takechi, M. Isobe, N. Nakajima, M. Osakabe, S. Takagi, T. Kondo, G. Matsunaga, K. Ohkuni, M. Sasao, Y. Yamamoto, S. Ohdachi, S. Sakakibara, H. Yamada, K. Y. Watanabe, D. S. Darrow, A. Fujisawa, M. Goto, K. Ida, H. Idei, H. Iguchi, S. Lee, S. Kado, S. Kubo, O. Kaneko, K. Kawahata, K. Matsuoka, T. Minami, S. Morita, O. Motojima, K. Narihara, S. Nishimura, N. Ohyabu, Y. Oka, S. Okamura, T. Ozaki, K. Sato, M. Sato, A. Shimizu, T. Shimojima, Y. Takeiri, K. Tanaka, T. Tokuzawa, K. Tsumori, I. Yamada, Y. Yoshimura, Chs and L. H. D. E. Groups, *Nuclear Fusion* **40** (2000) (7), p. 1349
- [22] T. Ido, M. Osakabe, A. Shimizu, T. Watari, M. Nishiura, K. Toi, K. Ogawa, K. Itoh, I. Yamada, R. Yasuhara, Y. Yoshimura, S. Kato and L. H. D. E. G. The, *Nuclear Fusion* **55** (2015) (8), p. 083024
- [23] X. D. Du, K. Toi, S. Ohdachi, M. Osakabe, T. Ido, K. Tanaka, M. Yokoyama, M. Yoshinuma, K. Ogawa, K. Y. Watanabe, T. Akiyama, M. Isobe, K. Nagaoka, T. Ozaki, S. Sakakibara, R. Seki, A. Shimizu, Y. Suzuki, H. Tsuchiya and L. H. D. E. G. the, *Nuclear Fusion* **56** (2016) (1), p. 016002
- [24] X. D. Du, K. Toi, M. Osakabe, S. Ohdachi, T. Ido, K. Tanaka, M. Yokoyama, M. Yoshinuma, K. Ogawa, K. Y. Watanabe, M. Isobe, K. Nagaoka, T. Ozaki, S. Sakakibara, R. Seki, A. Shimizu, Y. Suzuki, H. Tsuchiya and L. H. D. E. Group, *Physical Review Letters* **114** (2015) (15), p. 155003
- [25] S. Nishimura, *Physics of Plasmas* **22** (2015) (7), p. 072505

- [26] S. Nishimura, T. Nicolas and X. Du, *Fusion Engineering and Design* **109** (2016), pp. 1188–1192
- [27] K. Tanaka, C. Michael, L. Vyacheslavov, H. Funaba, M. Yokoyama, K. Ida, M. Yoshinuma, K. Nagaoka, S. Murakami, A. Wakasa, T. Ido, A. Shimizu, M. Nishiura, Y. Takeiri, O. Kaneko, K. Tsumori, K. Ikeda, M. Osakabe, K. Kawahata and L. H. D. E. Group, *Plasma and Fusion Research* **5** (2010), pp. S2053–S2053
- [28] K. Ida, Y. Sakamoto, M. Yoshinuma, H. Takenaga, K. Nagaoka, N. Hayashi, N. Oyama, M. Osakabe, M. Yokoyama, H. Funaba, N. Tamura, K. Tanaka, Y. Takeiri, K. Ikeda, K. Tsumori, O. Kaneko, K. Itoh, S. Inagaki, T. Kobuchi, A. Isayama, T. Suzuki, T. Fujita, G. Matsunaga, K. Shinohara, Y. Koide, M. Yoshida, S. Ide, Y. Kamada, L. H. D. E. G. the and J. T. T. the, *Nuclear Fusion* **49** (2009) (9), p. 095024
- [29] Y. Takeiri, O. Kaneko, K. Tsumori, M. Osakabe, K. Ikeda, K. Nagaoka, H. Nakano, E. Asano, T. Kondo and M. Sato, *Fusion Science and Technology* **58** (2010) (1), pp. 482–488
- [30] M. Goto, S. Morita, K. Sawada, T. Fujimoto, S. Yamamoto, J. Miyazawa, H. Yamada and K. Toi, *Physics of Plasmas* **10** (2003) (5), pp. 1402–1410
- [31] K. Ida, M. Yoshinuma, M. Goto, O. Schmitz, S. Dai, A. Bader, M. Kobayashi, G. Kawamura, C. Moon, Y. Nakamura and L. H. D. E. G. The, *Plasma Physics and Controlled Fusion* **58** (2016) (7), p. 074010
- [32] K. Ida, M. Yoshinuma, B. Wieland, M. Goto, Y. Nakamura, M. Kobayashi, I. Murakami and C. Moon, *Review of Scientific Instruments* **86** (2015) (12), p. 123514
- [33] S. Murakami, A. Fukuyama, T. Akutsu, N. Nakajima, V. Chan, M. Choi, S. C. Chiu, L. Lao, V. Kasilov, T. Mutoh, R. Kumazawa, T. Seki, K. Saito, T. Watari, M. Isobe, T. Saida, M. Osakabe, M. Sasao and L. H. D. E. Group, *Nuclear Fusion* **46** (2006) (7), p. S425
- [34] C. Michael, K. Tanaka, L. Vyacheslavov, A. Sanin, K. Kawahata and S. Okajima, *Plasma and Fusion Research* **2** (2007), pp. S1034–S1034
- [35] C. A. Michael, K. Tanaka, L. Vyacheslavov, A. Sanin and K. Kawahata, *Review of Scientific Instruments* **86** (2015) (9), p. 093503
- [36] Y. I. Kolesnichenko, S. Yamamoto, K. Yamazaki, V. V. Lutsenko, N. Nakajima, Y. Narushima, K. Toi and Y. V. Yakovenko, *Physics of Plasmas* **11** (2003) (1), pp. 158–170
- [37] S. Yamamoto, K. Toi, N. Nakajima, S. Ohdachi, S. Sakakibara, K. Y. Watanabe, M. Goto, K. Ikeda, O. Kaneko, K. Kawahata, S. Masuzaki, T. Morisaki, S. Morita, S. Murakami, K. Narihara, Y. Oka, M. Osakabe, Y. Takeiri, K. Tanaka, T. Tokuzawa, K. Tsumori, H. Yamada, I. Yamada and K. Yamazaki, *Physical Review Letters* **91** (2003) (24), p. 245001
- [38] Y. I. Kolesnichenko, V. V. Lutsenko, H. Wobig and V. Yakovenko, *Physics of Plasmas* **9** (2002) (2), pp. 517–528
- [39] L. H. D. E. Group, K. Toi, F. Watanabe, T. Tokuzawa, K. Ida, S. Morita, T. Ido, A. Shimizu, M. Isobe, K. Ogawa, D. A. Spong, Y. Todo, T. Watari, S. Ohdachi, S. Sakakibara, S. Yamamoto, S. Inagaki, K. Narihara, M. Osakabe, K. Nagaoka, Y. Narushima, K. Y. Watanabe, H. Funaba, M. Goto, K. Ikeda, T. Ito, O. Kaneko, S. Kubo, S. Murakami, T. Minami, J. Miyazawa, Y. Nagayama, M. Nishiura, Y. Oka, R. Sakamoto, T. Shimozuma, Y. Takeiri, K. Tanaka, K. Tsumori, I. Yamada, M. Yoshinuma, K. Kawahata and A. Komori, *Physical Review Letters* **105** (2010) (14), p. 145003
- [40] M. Isobe, M. Osakabe, T. Ozaki, M. Nishiura, P. Goncharov, E. Veshchev, K. Ogawa, K. Nagaoka, K. Saito and S. Murakami, *Fusion Science and Technology* **58** (2010) (1), pp. 426–435
- [41] P. R. Goncharov, T. Ozaki, S. Sudo, N. Tamura, T. Group, L. E. Group, E. A. Veshchev, V. Y. Sergeev and A. V. Krasilnikov, *Review of Scientific Instruments* **77** (2006) (10), p. 10F119
- [42] M. Osakabe, T. Yamamoto, Y. Takeiri, T. Mutoh, E. Asano, K. Ikeda, K. Tsumori, O. Kaneko, K. Kawahata, N. Ohyabu, O. Motojima and L. E. Group, *Review of Scientific Instruments* **72** (2001) (1), pp. 788–791
- [43] K. Saito, R. Kumazawa, T. Seki, K. Hirosh, G. Nomura, F. Shimpo, H. Igami, M. Isobe, K. Ogawa, K. Toi, M. Osakabe, M. Nishiura, T. Watanabe, S. Yamamoto, M. Ichimura, T. Mutoh and L. H. D. E. Group, *Plasma Science and Technology* **15** (2013) (3), p. 209
- [44] G. T. Shekar, G. S. Yun, J. Leem, H. K. Park, K. W. Kim, T. Akiyama and S. G. Lee, *Plasma Physics and Controlled Fusion* **58** (2016) (6), p. 065003
- [45] K. Ida and N. Nakajima, *Physics of Plasmas* **4** (1997) (2), pp. 310–314
- [46] H. P. Summers, *The ADAS User Manual, version 2.6*, Report (2004), URL: <http://www.adas.ac.uk>
- [47] B. Lehnert, *Physica Scripta* **12** (1975) (6), p. 327
- [48] P. M. L. NIST, *Electron-Impact Cross Sections for Ionization and Excitation Database*, URL: <https://www.nist.gov/pml/electron-impact-cross-section>
- [49] R. Makino, K. Tanaka, S. Kubo, M. Yokoyama, M. Shoji, K. Ida, M. Goto, R. Seki, T. Ido and H. Yamada, *Heat and particle transport in hydrogen and helium ECH plasmas on LHD*, in *41st EPS Conference on Plasma Physics*
- [50] Y. Feng, F. Sardei and J. Kisslinger, *Journal of Nuclear Materials* **266** (1999), pp. 812–818
- [51] M. Goto, K. Sawada, K. Fujii, M. Hasuo and S. Morita, *Nuclear Fusion* **51** (2011) (2), p. 023005
- [52] A. Y. Wong, R. W. Motley and N. D’Angelo, *Physical Review* **133** (1964) (2A), pp. A436–A442
- [53] X. . Du, K. Toi, S. Ohdachi, K. . Watanabe, H. Takahashi, Y. Yoshimura, M. Osakabe, R. Seki, T. Nicolas, H. Tsuchiya, K. Nagaoka, K. Ogawa, K. Tanaka, M. Isobe, M. Yokoyama, M. Yoshinuma, S. Kubo, S. Sakakibara, T. Bando, T. Ido, T. Ozaki, Y. Suzuki, Y. Takemura and L. H. D. E. Group, *Physical Review Letters* **118** (2017) (12), p. 125001
- [54] T. Bando, S. Ohdachi and al, *to Be submitted Nucl. Fusion*